



NTNU – Trondheim
Norwegian University of
Science and Technology

Sliding Stability of Lightweight Concrete Dams

Development of Numerical Models

Øystein Eltervaag

Civil and Environmental Engineering

Submission date: June 2013

Supervisor: Kjell H. Holthe, KT

Co-supervisor: Leif Lia, IVM

Norwegian University of Science and Technology
Department of Structural Engineering



MASTEROPPGAVE

Student: ØYSTEIN ELTERVAAG

TITTEL: GLIDESIKKERHET FOR LETTE
BETONGDAMMER

-ETABLERING AV NUMERISK REGNEMODELL

1 BAKGRUNN

Betongdammer skal være både velte- og glidesikre. Vi har per i dag ikke god nok kunnskap om hvordan ruhet, fortanning og heft påvirker den reelle skjærstyrken mellom betongdam og fjellfundament. Vi står derfor i fare for å bygge og fornye konstruksjoner uten å kjenne den reelle kapasiteten mot gliding. Det kan føre til konstruksjoner som enten ikke er sikre nok eller er unødvendig kostbart dimensjonert.

Med eksisterende beregningsmetoder basert på gjennomsnittsverdier av spenning, styrke og helling er det ikke mulig å få et tilfredsstillende svar på betongdammers reelle sikkerhetsfaktor mot glding S_g . Det er derfor nødvendig å utføre supplerende beregninger, basert på ordinær statikk/fasthetslære eller på numeriske regnemodeller. Slike metoder og

modeller kan gi interessante svar, spesielt vurdert opp mot dagens forenklete beregningsmetoder.

Våren 2012 ble det gjennomført direkte skjærtester på prøvestykker av betong og granitt ved LTU (Luleå). Dette materialet muliggjør kalibrering av en numerisk beregningsmodell, og danner dermed grunnlaget for dette arbeidet.

2 ICOLD

Mye av arbeidet med dammer og damsikkerhet i verden organiseres innenfor ICOLD – International Commission on Large Dams. Det finnes egne grupper som arbeider med betongdammer og stabilitet og det finnes en stor mengde litteratur på området. Det er naturlig at ICOLD blir bindeleddet ut mot internasjonal praksis og at nivået på litteraturen publisert i ICOLD danner basis for oppgaven.

3 GJENNOMFØRING AV OPPGAVEN

Arbeidet med oppgaven kan deles inn i fire faser:

3.1 Bakgrunnsmateriale

Resultat fra laboratorie-forsøk, tidligere rapporter, tegninger, artikler, bøker, programdokumentasjon, materialeegenskaper m.m. danner bakgrunnsmateriale for oppgaven. Materialet skal lede fram mot beregninger som kan vise hvordan krefter og spenninger opptrer ved et glidebrudd. Eksisterende metoder og modeller som f.eks. FEM-modeller må vurderes dersom det er tilgjengelig. Enkle modeller for beregninger på oversiktsnivå må også vurderes. Norske forhold og regelverk skal tas hensyn til i oppgaven, slik at det som vurderes har sterk relevans til lette platedammer i Norge.

3.2 Etablering av regnemodeller

Situasjoner og forutsetninger som skal regnes på må defineres og verifiseres. Det må lages en plan for hvilke metoder og modeller som skal benyttes til beregningene. I samarbeid med Statkraft og NORUT i Narvik skal det etableres et arbeid som fører fram til hvordan den reelle sikkerhetsfaktoren

kan finnes og hvor stor denne er. Ulike forutsetninger og situasjoner skal regnes i modellene, slik at resultatene blir relevante for norske platedammer.

3.3 Resultat

Resultat fra beregningene må sammenlignes med kjente forhold og det må vises hvordan dette påvirker sikkerheten til en damkonstruksjon. Det må i hovedsak skilkes mellom situasjonene:

1. Tilfredsstillende sikkerhet
2. Ikke tilfredsstillende sikkerhet, krever tiltak
3. Brudd på konstruksjonen

3.4 Konkludering

Arbeidet skal lede fram mot en regnemodell som inkluderer alle relevante forhold ved et glidebrudd. Arbeidet skal også vise hvordan sikkerheten vil endre seg med endrede forutsetninger og vilkår. Det må vises hvordan resultatene fra beregninger gir føringer for valg av eventuelle tiltak for forsterking, der dette er nødvendig med tanke på damsikkerheten.

4 KONTAKTPERSONER

NTNU	Kjell H. Holthe, Professor, formell veileder
NTNU	Leif Lia, Professor, medveileder
NORUT	Gabriel Sas, Dr.Ing, medveileder
Statkraft	Trond Bjertnes og Anne Marit Ruud

Det vil i tillegg være aktuelt å knytte kontakt med fagmiljø som er aktive innenfor studier av betongkonstruksjoner som Sintef Betong, EnergiNorge, NVE m.fl.

5 RAPPORTFORMAT, REFERANSER OG ERKLÆRING

Oppgaven skal skrives i et tekstbehandlingsprogram slik at figurer, tabeller, foto osv. får god rapportkvalitet. Rapporten skal inneholde et sammendrag, en innholdsliste, en liste over figurer og tabeller, en litteraturliste og opplysninger om andre relevante referanser og kilder. Oppgaven skal leveres i B5 format som pdf i DAIM og trykkes i tre eksemplar som leveres faglærer/institutt.

Sammendraget skal ikke overstige 450 ord og skal være egnet for elektronisk rapportering.

Masteroppgaven skal ikke leveres senere enn mandag 10. juni 2013.

Trondheim, 15. januar 2013

ABSTRACT

Sliding failure of lightweight concrete dams occur if the horizontal forces subjected to the dam exceeds the shear capacity of one or more sliding planes in the dam's structure or foundation. Thus, sliding is a result of a shear failure in the dam or foundation.

The scope of this Thesis is to investigate how surface roughness influences the shear capacity of possible sliding planes in lightweight concrete dams, and in this way affect the stability of dams regarding sliding failure. By studying physical shear tests conducted by Simen Liahagen in 2012 it has been found that the shear capacity of a sliding plane is governed by two failure mechanisms.

For a bonded interface, sliding is a result of a material failure in one or both of the adjoining materials. For an un-bonded interface, the capacity might be governed by both the frictional capacity of the roughness at the interface and local material failure in parts of the roughness. From the analyses of Liahagen's shear tests it was found that what failure mode that governs the capacity is dependent on both the normal stress and the inclination of the interface roughness.

The shear tests indicate that if the surface roughness is not cut-off, it contributes to the shear capacity in two ways. Firstly, the macro-roughness, or asperities, along the sliding plane increase the shear capacity by tilting the plane of the actual sliding failure. Secondly, the micro roughness along the asperities is cut off for a sliding failure. This contributes to the total shear capacity more than tilting the sliding plane.

By comparing the theoretical formulations for shear capacity used in today's guidelines to the shear tests it has been found that this theory do not represent the shear capacity sufficiently. Trough finite element analyses a better representation of the tests has been achieved, especially regarding the influence of micro roughness.

The approach from analyzing the tests has been further developed to enable assessment of the sliding stability of a full scale dam. The results show that the roughness gives a notable increase in the stability for sliding. However, further tests and calibration are needed to utilize the full potential of this method.

SAMMENDRAG

Glidebrudd i lette betongdammer forekommer hvis de horisontale kreftene dammen blir utsatt for overstiger skjærkapasiteten langs mulige glideplan i dammen eller fundamentet. Dermed kan glidning ses på som et resultat av skjærbrudd i damkonstruksjonen.

Målet med denne oppgaven er å undersøke hvordan overflateruhet langs potensielle glideplan i en betongdam påvirker skjærkapasiteten, og på denne måten påvirker dammens totale glide-stabilitet. Gjennom studier av fysiske skjærtester gjennomført av Simen Liahagen i 2012 er det oppdaget at skjærkapasiteten langs et glideplan styres av to bruddmekanismer.

For et glideplan med heft vil glidning oppstå som et resultat av et materialbrudd langs planet eller i et av planets tilstøtende materialer. For et glideplan uten heft, bestemmes kapasiteten av både motstanden mot gliding over ruheten og lokale materialbrudd i deler av denne overflateruheten. Liahagen's tester indikerer at hvilken av disse mekanismene som bestemmer kapasiteten avhenger både av normalspenningen langs planet men også av helningsvinkelen til ruheten.

Skjærtestene viser at dersom ikke ruheten skjæres av, vil den øke kapasiteten på to måter. For det første vil ruheten øke helningsvinkelen til det faktiske glideplanet. For det andre vil mikro-ruhet langs overflaten bli skåret av, som øker den totale skjærkapasiteten ytterligere.

En sammelinkning av det teoretiske grunnlaget om brukes for å beregne glide stabiliteten av betongdammer i dag med de fysiske testene viser at teorien ikke representerer den faktiske skjærkapasiteten tilstrekkelig. Elementanalyse viser bedre overensstemmelse med testene, spesielt med tanke på innvirkningen av mikroruhet.

Metoden fra analyseringen av testene har blitt videreutviklet for å kunne vurdere glide stabiliteten til en fullskala dam. Resultatene viser at ruheten bidrar til vesentlig økning i glide stabiliteten, men det kreves flere tester og ytterligere kalibrering for å utnytte denne metodens fulle potensial.

PREFACE

This Thesis has been written by the signatory as the final work of my Master's Degree at Department of Structural Engineering at the Norwegian University of Science and Technology (NTNU).

The subject for this thesis was chosen to make use of my background from both computational mechanics and hydro power development. This has proved to be an ambitious approach and led to numerous challenges in both fields. However, overcoming these challenges has led to an increased understanding of both numerical modeling and shear failure development that I would not have been without.

I would like to express my gratitude to my supervisors Professor Kjell Holthe and Professor Leif Lia for making it possible to write this Thesis as a collaboration between Department of Structural Engineering and Department of Hydraulic and Environmental Engineering at NTNU.

Special thanks are acknowledged to my co-supervisor Dr. Gabriel Sas at NORUT/LTU. Trough his supervision he has not only increased my understanding of numerical modeling, but also kept me motivated to charge trough the difficulties and never give up. Thanks are also acknowledged to Dr. Dobromil Pryl at Cervenka Consulting for his kind replies to my numerous questions.

Finally, I would like to thank EnergiNorge for financial support. This has enabled me to travel which greatly has increased the quality of my supervision.

Trondheim, June 10th 2013

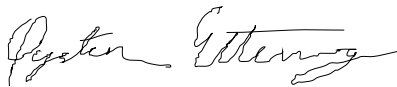
X 
Øystein Eltervaag

TABLE OF CONTENTS

ABSTRACT	i
SAMMENDRAG	ii
PREFACE	iii
FIGURE LIST	ii
TABLE LIST	vii
1. INTRODUCTION	1
1.1 Background	1
1.2 Objectives	2
1.3 Method	2
1.4 Extent and limitations	2
1.5 The structure of this Thesis	3
2. PRECEDING WORK	4
2.1 Stølen's Master's Thesis	4
2.2 Liahagen's Master's Thesis	8
2.3 Recap of FE-analyses from the Project	11
3. THEORY	14
3.1 Assessing stability towards sliding	14
3.1.1 Shear capacity and failure mechanisms	15
3.1.2 New methods for assessing stability towards sliding	19
3.2 Alternative formulations	21
4. PRELIMINARY ANALYSES	22
4.1 Finding the basic friction angle from test 4.2	22
4.2 Failure of test series 3	25
4.3 Failure of test series 2	28
4.4 Failure of test series 1	32
4.5 Failure of tests with bond	34
4.6 Discussion	35
5. NUMERICAL MODELS OF SLIDING STABILITY	37

5.1	Geometry	37
5.2	Modeling contact in ATENA	39
5.3	The material models.....	44
5.3.1	The concrete material model	45
5.3.2	The steel material model	47
5.4	Loading and Boundary Conditions	48
5.5	Meshing	50
5.6	Analysis steps	52
5.7	Ill-conditioning	53
5.8	Modeling a full scale dam.....	56
6.	RESULTS AND DISCUSSION	61
6.1	Comparison of Liahagen's tests.....	61
6.1.1	Test 4.2.....	62
6.1.2	Test series 3.....	62
6.1.3	Test series 2.....	64
6.1.4	Test series 1.....	66
6.1.5	Tests with bond	70
6.2	Discussion of the numerical results.....	71
6.3	Results from full scale dam analyses	73
7.	CONCLUSIONS	77
	REFERENCES	- 1 -
	DIGITAL APPENDIX	- 3 -
	APPENDIX A	- 5 -
	APPENDIX B	- 10 -
	APPENDIX C	- 12 -
	APPENDIX D	- 18 -
	APPENDIX E.....	- 19 -
	APPENDIX F	- 24 -
	APPENDIX G	- 26 -

FIGURE LIST

Figure 2.1: Element mesh (Stølen 2012).	5
Figure 2.2: Plasticization of the interface (Stølen 2012).	6
Figure 2.3: Load-Displacement for dam-section with rock-bolts (Stølen 2012).	6
Figure 2.4: Load - Displacement without rock-bolts (Stølen 2012).	7
Figure 2.5: Shear stress at dam base (Stølen 2012).	7
Figure 2.6: The test rig at LTU (Liahagen 2012).	8
Figure 2.7: Profiles of test samples (Liahagen 2012)	9
Figure 2.8: Loading of the models.....	12
Figure 2.9: Comparison of FEM results and test results for test 3.3.....	12
Figure 2.10: Comparison of FEM results and test results for test 4.2.....	13
Figure 3.1: Patton's bi-linear failure criterion (Johansson 2009).	16
Figure 3.2: Principle sketch of an idealized 2D asperity (Johansson 2009).	17
Figure 3.3: Different failure modes for an idealized asperity (Johansson 2009).	18
Figure 4.1: Load - displacement relations for test 4.2 (Liahagen 2012).	23
Figure 4.2: Load-displacement relations for test series 3 (Liahagen 2012).	25
Figure 4.3: Load-displacement relations for test series 2 (Liahagen 2012).	28
Figure 4.4: Sliding and shearing failure capacity for test series two.	29
Figure 4.5: Load-displacement relations for test series 1 (Liahagen 2012).	32
Figure 4.6: Load-displacement relation for test with bond (Liahagen 2012).	34
Figure 5.1: 2D geometrical model of test 3.3	38
Figure 5.2: Typical interface behavior in shear and tension (Cervenka et. Al 2012). ..	40
Figure 5.3: Sketch of interface elements in ATENA (Cervenka et. Al 2012).	41
Figure 5.4: Material parameters for the Interface material for test 3.3 in GiD.	43
Figure 5.5: Illustration of the material allocation in GiD (test2.3).	45
Figure 5.6: Uniaxial concrete behavior (Cervenka et. Al 2012).	46
Figure 5.7: Material description for steel in ATENA	47
Figure 5.8: Loading and BC's of interval 1 for test 3.3.	48
Figure 5.9: Loading and BC's of interval 2 for test 3.3.	50
Figure 5.10: Mesh of test 2.2.	51
Figure 5.11: Interval Data.	52
Figure 5.12: Influence of interface material stiffness for test 4.2.	55
Figure 5.13: Dam Ipto (Sweco 2007)	57
Figure 5.14: Model of Dam Ipto.....	58
Figure 5.15: Imposed conditions in load interval one.	60
Figure 6.1: Test 4.2.....	62
Figure 6.2: Test 3.1.....	63
Figure 6.3: Test 3.2.....	63
Figure 6.4: Test 3.3.....	64
Figure 6.5: Test 2.1.....	65

Figure 6.6: Test 2.2.....	65
Figure 6.7: Test 2.3.....	66
Figure 6.8: Cracking of concrete material for test 1.1	67
Figure 6.9: Material failure for test 1.4.....	67
Figure 6.10:Test 1.1.....	68
Figure 6.11: Test 1.2.....	68
Figure 6.12: Test 1.4.....	69
Figure 6.13: Test 4.1H.....	70
Figure 6.14: Results from analyses of dam Ipto.	73
Figure 6.15: Interface shear stresses for analysis C (numbers in MPa).	74

TABLE LIST

Table 2.1: Test results from Liahagen (2012)	10
Table 2.2: Material parameters.	11
Table 4.1: Comparison of peak shear capacity for test series 3.	25
Table 4.2: Comparison of residual shear capacity for test series 3.	26
Table 4.3: Cohesive values for micro roughness for test series 3.	27
Table 4.4: Comparison of peak shear capacity for test series 2.	30
Table 4.5: Comparison of residual shear capacity for test series 2.	31
Table 4.6: Cohesive values for micro roughness for test series 2.	31
Table 4.7: Comparison of peak shear capacity for test series 1.	33
Table 4.8: Cohesive values for macro roughness for test series 1.	33
Table 4.9: Results from hand calculations	35
Table 5.1: Material parameters for concrete material models	47
Table 5.2: Loading of the models.	49
Table 5.3: Interface stiffness values	55
Table 5.4: Shear capacity from equation 5.9.	56
Table 5.5: Material parameters for C 20/25 concrete in ATENA.....	58
Table 5.6: Interface parameters	59
Table 5.7: Applied loads of the dam section.	60
Table 6.1: Error in peak shear capacity from the numerical models.	71
Table 6.2: Factor of safety from finite element analyses.	73

1. INTRODUCTION

This Master's Thesis is a continuation of the work done in the author's specialization project: "Sliding Stability of Lightweight Concrete Dams – Contribution from Surface Roughness". The focus in the project was to establish the theoretical foundations for sliding stability. In addition a study on the possibility of applying finite element analyses on sliding stability problems was carried out.

The project forms the literature study for this Thesis, in which the focus lies on application of finite element analyses to sliding stability problems.

1.1 Background

In Norway, the stability of a dam is reconsidered every 15 or 21 years, depending on the consequence of a dam break for the given dam. The purpose of this reconsideration is to assess the constructional safety of a dam with respect to accepted safety levels. In the past 40-50 years, since the large hydropower development époque in Norway, the level of required safety has increased. This result in situations where dams constructed in this period no longer are considered stable and expensive rehabilitations are needed.

Trough the work with the specialization project it was discovered that sliding failure is governed by two different mechanisms. Sliding failure occurs either as a result of exceeding the frictional capacity along an unbounded sliding plane, or as a result of shear-failure in intact material. The Mohr-Coulomb criterion used in today's guidelines is only able to describe the mechanism of material failure, and is therefore not sufficient for assessing the sliding stability of concrete dams.

Furthermore the sliding stability is today only assessed trough simplified hand calculations where the shear and normal stresses are averaged over the entire sliding plane. There are reasons to believe that this method do not represent the sliding failure with sufficient realism.

1.2 Objectives

The general scope for this Master's Thesis is to develop a better approach to sliding stability assessments of lightweight concrete dams. The objective is to further analyze how a sliding failure elapse, what mechanisms that govern shear capacity, and to investigate how these mechanisms can be included in the stability calculations.

1.3 Method

The method for obtaining more realistic stability assessments for sliding failure consists of three steps. Initially the governing mechanisms for sliding failure are investigated trough analyses of twelve shear tests conducted by Simen Liahagen in 2012. The shear capacity of these tests is then compared to the theoretical foundations obtained through the author's Project work to understand and quantify the effect of the different mechanisms. From this analysis the properties of the sliding plane is found.

The properties of the sliding plane are used as input parameters in finite element analyses. By comparing the results from these analyses to the actual results from the tests the quality of the numerical models can be assessed. The numerical models developed from the tests are in turn applied to a full scale dam to show how this method provides a more realistic capacity for sliding failure.

1.4 Extent and limitations

Due to late arrival of the license for the finite element software ATENA (mid April) the focus has been on establishing running models. Achieving trustworthy results from these numerical models proved to be much more time-consuming than anticipated. Thus, only the effect of surface roughness is studied. Contribution from rock bolts, or combinations of bonded and unbonded sliding planes are not investigated.

In total, eleven of the twelve shear tests from Liahagen (2012) are analyzed, along with three analyses of a section of dam Ipto.

1.5 The structure of this Thesis

The Thesis consists of seven chapters. In chapter 2 preceding Master's Theses on the subject are presented. This chapter also contains a brief summary of the numerical analyses conducted in the author's project work. The theoretical foundations for sliding failure and the criteria for shear capacity found through the literature study in the author's project work are presented in chapter 3.

Chapter 4 contains preliminary analyses of Liahagen's tests. Pictures from the tests have been thoroughly studied in order to capture how the failure precedes, and what failure mode governs the shear capacity of the different tests. A comparison between the formulations for shear capacity found in chapter 3 and the test results are carried out. Based on this, an approach for how to describe the observed shear capacity for these tests are developed.

The development of the numerical models is described thoroughly in chapter 5. This chapter contains descriptions of the material models, the geometry and loading of the models, and the troubleshooting of the analyses.

The results are presented and discussed in chapter 6. By comparing the numerical results to the results of the actual tests the discrepancies become visible. By analyzing the source of these discrepancies the usability of the numerical models can be further investigated.

In the final chapter the conclusions from the work with this Thesis are presented along with suggestions for further work.

2. PRECEDING WORK

This chapter contains a brief presentation of preceding work on the topic. The purpose is to shed light on the work done by previous students at NTNU, and in such a way put this Thesis into context.

In the fall of 2009 Olav Jørstad wrote a specialization project on sliding stability of buttress dams at IVT, NTNU. Based on his findings two Master's Theses on the topic were initiated in 2012. One was written by Peter Stølen (Stølen 2012), the other by Simen Liahagen (Liahagen 2012). The scope for these two Theses was to investigate the influence of bond and surface roughness on the stability for sliding of concrete dams, through shear tests and numerical models.

2.1 Stølen's Master's Thesis

The scope for this Thesis was to assess the sliding stability of Målset dam, a buttress dam in the Sogn og Fjordane county in Norway. The stability was assessed through hand calculations and finite element analyses (FE-analyses).

In his Thesis, Stølen analyzed several sections of the dam which is considered unstable by the calculation methods used today. The sliding stability was reassessed using the shear friction method, the limit equilibrium method, multiple wedge analyses and combined sliding and overturning method. These methods are thoroughly described in Stølen's Master's Thesis (2012) and also in Jørstad (2009). A brief description is given in APPENDIX A.

The results of the hand calculations showed that the dam does not satisfy the acquired safety levels for sliding stability. This is in line with reassessments of the dam's stability conducted in 2006 by Norconsult, although the results of these calculations are somewhat more conservative. The results from the different calculation methods gave corresponding results for sliding planes with low inclinations, but differed for sliding planes with high inclination.

The numerical modeling was performed using the Check finite element software ATENA, which is also used in this Thesis. A description of ATENA is given in chapter 5.

One section (Section 4) of the dam was chosen as a reference for numerical modeling. This section has a height of 6.7 meters, which makes it very interesting with respect to contribution from rock bolts¹. The dam and foundation was modeled with linear 2D triangle-elements with one integration point. For the interface between the dam and the foundation linear rectangular contact-elements with two integration points were used. The mesh is showed in figure 2.1 below. The reinforcement and rock bolts were modeled as 1D-elements. The material parameters used in this model is presented in APPENDIX B.

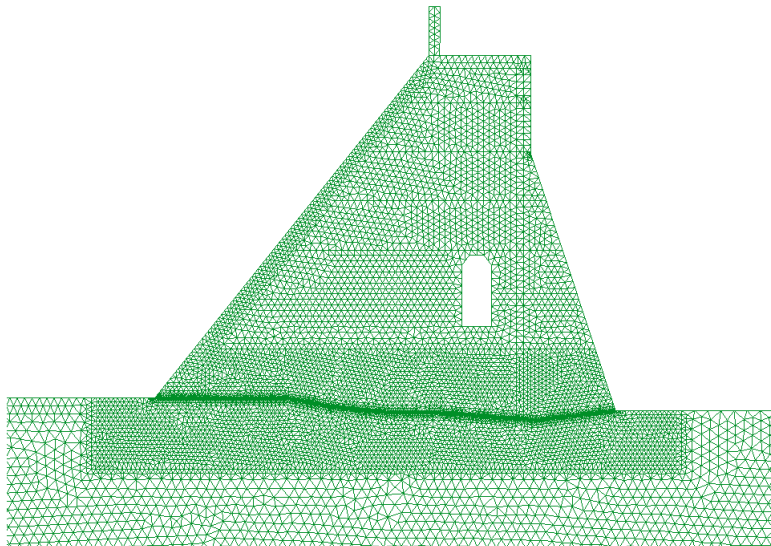


Figure 2.1: Element mesh (Stølen 2012).

The loading of the model consisted of the gravitational load of the dam, the hydrostatic water pressure, ice forces and an uplift pressure along the base of the dam. The uplift pressure proved hard to model, but this was cleverly

¹ According to the Norwegian guidelines for concrete dams, contribution from rock bolts in the stability calculations are only allowed for dam sections that are less than 7 meters tall (NVE 2005).

² In the tables in Liahagen's Thesis (and Eltervaag 2012) this value is printed as 30

PRECEDING WORK

solved by reducing the density of the concrete plate on the upstream end of the dam.

The stability was assessed by increasing the hydrostatic load until the interface material became completely plasticized. The maximum hydrostatic load divided by the standard hydrostatic load was interpreted as the factor of safety towards sliding. Due to complications with ATENA only analyses of interfaces with bond was conducted. The plasticization of the interface is shown in figure 2.2.

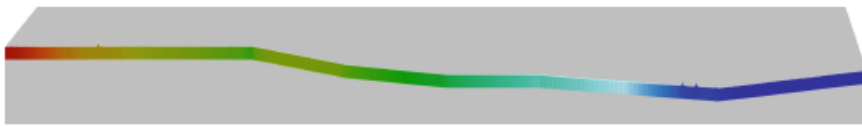


Figure 2.2: Plasticization of the interface (Stølen 2012).

A complete plasticization of the interface was interpreted as a failure in the bond between the dam and the foundation. The results were presented in load – displacements graphs as shown in figure 2.3 and 2.4 below. The graphs show the relationship for a dam-section with a cohesive parameter of 0.1 MPa both with and without contribution from rock-bolts.

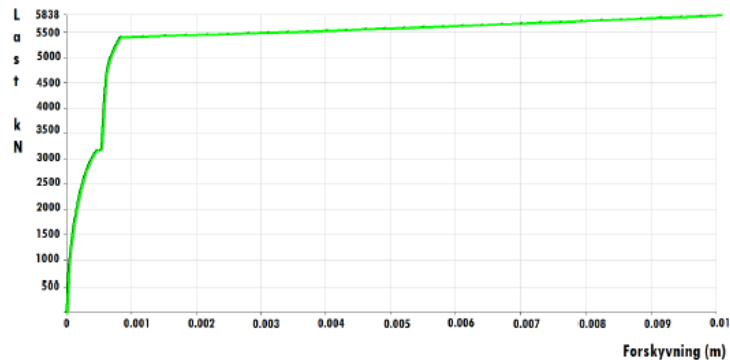


Figure 2.3: Load-Displacement for dam-section with rock-bolts (Stølen 2012).

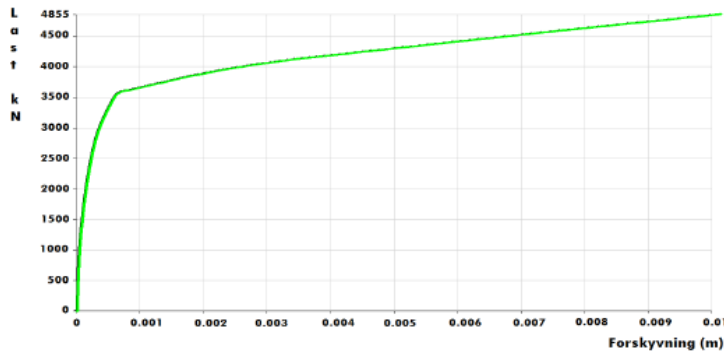


Figure 2.4: Load - Displacement without rock-bolts (Stølen 2012).

These results are interesting for two reasons. Firstly they indicate that rock-bolts will contribute to an increased sliding stability, and secondly they show that the dam will have some rest capacity after the bond is broken. Stølen explains this rest capacity as dry friction, which is very much in line with the theory first presented by Patton (1966) (see Chapter 3).

Contribution from surface roughness was not directly analyzed. However, the shear-stress distribution at the dam base after bond failure was studied. For all cases Stølen observed a stress concentration where the foundation is tilted upwards, as shown in figure 2.5 below. This indicates that the surface roughness will influence the rest capacity of the dam.

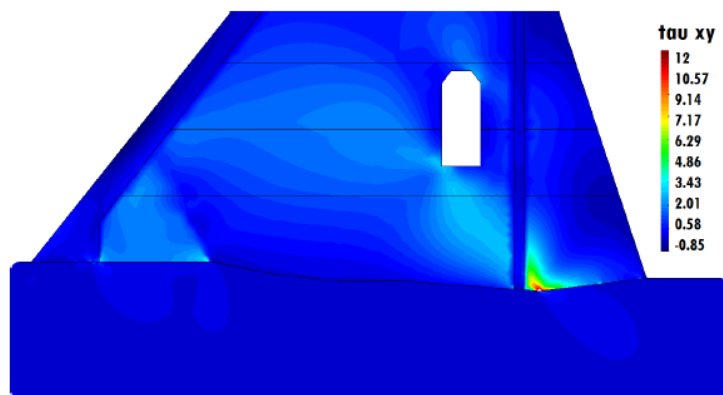


Figure 2.5: Shear stress at dam base (Stølen 2012).

2.2 Liahagen's Master's Thesis

During his Master's Thesis Simen Liahagen conducted twelve direct shear tests at Luleå Tekniska Univeristet (LTU). In these tests, granite samples were slid against concrete samples under a constant normal pressure.

The test rig consists of a rigid steel frame with dimension 2.5 by 2.5 meters. This frame supports a vertically mounted hydraulic jack and the lower part of the so called "shear box" in figure 2.6. The shear force is applied by two horizontally mounted jacks to the upper part of the shear box. This system (the red part in figure 2.6) is connected to the steel frame by springs which allows the moving parts to rotate approximately 10° relative to the shear direction. The jacks are able to provide a force of 500kN horizontally and vertically to the shear box (Liahagen 2012).

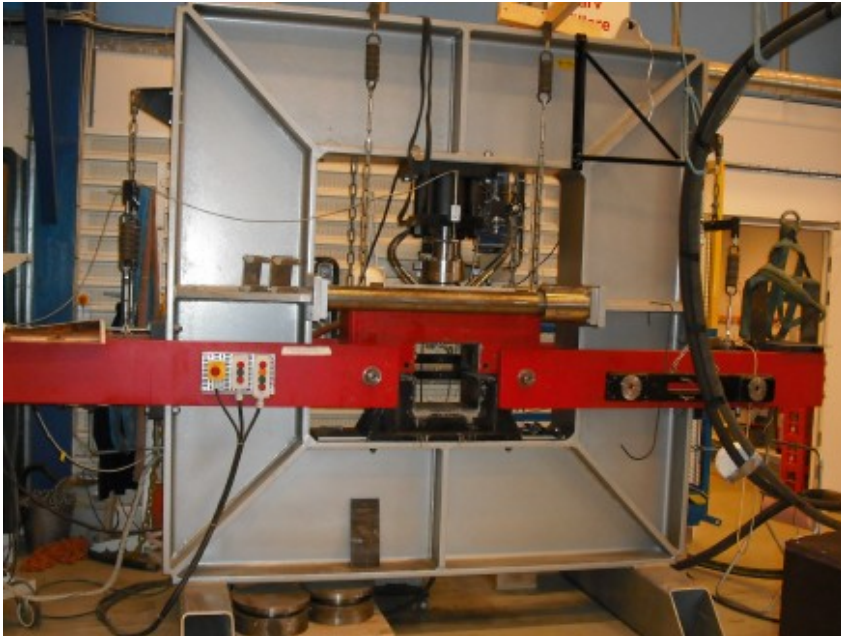


Figure 2.6: The test rig at LTU (Liahagen 2012).

The internal dimensions of the shear box's two parts is 285 x 270 x 130mm (l x b x h). To mount a sample in the shear box it is casted in a form to match the exact dimensions of the box.

The samples had the following dimensions: 240 x 240 x 130mm (l x b x h). The geometry of the interface between the rock and concrete is shown in figure 2.7. Pictures of the samples studied in this report are presented in APPENDIX C.

The compressive strength of the granite was 283 MPa. The concrete was casted on top of the rock samples, and by applying a thin plastic foil to the rock samples, bond was prevented in ten of the twelve samples. The concrete was mixed at site, and had a compressive strength of 58 MPa.

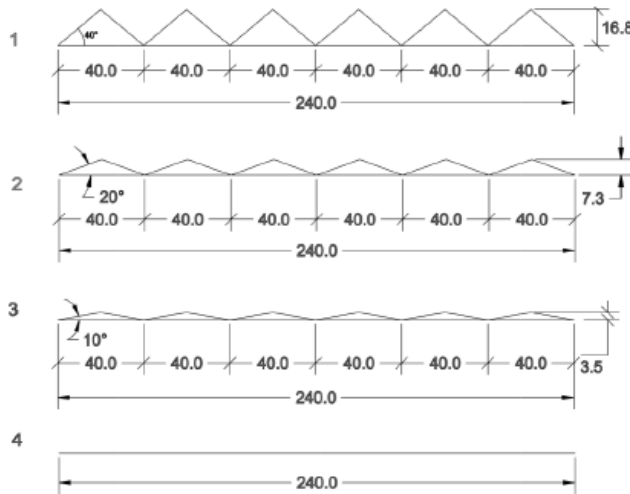


Figure 2.7: Profiles of test samples (Liahagen 2012).

The tests were conducted with four samples with geometry 1, three samples with geometry 2 and 3 respectively, and two samples with geometry 4. Two of the tests, one with geometry 1 and one with geometry 4 was conducted with adhesive bond. The results are shown in table 2.1 below

PRECEDING WORK

Table 2.1: Test results from Liahagen (2012).

Sample	i [°]	N [kN]	V [kN]	δ_H [mm]	σ_n [MPa]	τ_{max} [MPa]	ϕ_{max} [°]	δ_{Hmax} [mm]	Notes
1.1	40	27.52	90.53	4.00	0.48	1.57	73.08	15.23	
1.2	40	46.91	131.19	3.03	0.81	2.28	70.32	15.44	
1.3H	40	72.47	299.17	3.58	1.26	5.20	76.41	5.07	Bond
1.4	40	68.49	183.42	1.44	1.19	3.18	69.52	26.34	
2.1	20 ²	27.57	50.74	6.39	0.48	0.88	61.48	24.99	
2.2	20	47.77	100.59	2.86	0.83	1.75	64.60	21.98	
2.3	20	68.36	162.83	2.30	1.19	2.83	67.23	20.07	
3.1	10	24.82	35.38	9.78	0.43	0.61	54.95	33.16	
3.2	10	45.98	58.70	6.55	0.80	1.02	51.93	32.94	
3.3	10	67.65	85.43	2.83	1.17	1.48	51.63	33.23	
4.1H	0	67.85	240.00	2.49	1.18	4.17	74.24	14.59	Bond
4.2	0	67.23	52.04	33.23	1.17	0.90	37.74	33.23	

Where i is the asperity inclination, N and V are the normal and horizontal forces respectively, δ_H , is the horizontal displacement at peak shear capacity, σ_n , is the normal stress, τ_{max} is the peak shear capacity, and δ_{Hmax} is the total horizontal displacement. The ϕ_{max} value has been calculated from the measured normal and shear forces as

$$\phi_{max} = \tan^{-1}\left(\frac{V}{N}\right) \quad (2.1)$$

By studying this parameter, it is clear that the surface roughness contributes to the shear capacity, especially for joints without bond.

Unfortunately the work of Liahagen was heavily delayed due to complications in receiving the rock samples. The result of this delay was a very limited timeframe for analyzing and interpreting the results. This makes it hard to utilize the full potential of these shear tests in further studies.

² In the tables in Liahagen's Thesis (and Eltervaag 2012) this value is printed as 30 degrees. However, from the surrounding text and figures it appears that the samples actually had an inclination of 20 degrees.

2.3 Recap of FE-analyses from the Project

In the specialization project simple 2D FE-analysis was conducted using the finite element software ABAQUS developed by Dassault Systèmes. The analyses were based on the shear test 3.3 and 4.2 from Simen Liahagen (2012) described in section 2.2.

These two tests were chosen for modeling due to their relative simple geometry, and because they were run with equal normal pressure. The purpose was to assess whether FE-analyses was able to present sliding over a rough surface.

The geometry of the samples used in the shear tests were modeled as 2D plane parts in ABAQUS. The models were meshed with modified quadratic triangle elements (CPS6M). The element size was set to 5 mm. Both rock and concrete was modeled with the Concrete Damaged Plasticity material model.

The material parameters were based on sample descriptions by Liahagen (2012), however values for all the needed parameters were not found. Therefore additional values have been estimated based on generalized approximations from Eurocode 2 and Nilsen and Thidemann (1993). The material properties are presented in table 2.2.

Table 2.2: Material parameters.

Material	Concrete	Rock
Young's Modulus [GPa]	33	100
Poisson's Ratio	0.2	0.2
Compressive Yield Stress [MPa]	30	200
Compressive Failure Stress [MPa]	58	280
Inelastic strain at compressive failure	0.0035	0.001
Tensile Failure Stress [MPa]	3.8	4.0
Dilation Angle ³	31	35

The models were loaded by a normal pressure on top and a prescribed deformation field on the upper left side. The lower parts of the models were constrained vertically along the base and horizontally along the left side. Contact was modeled using finite sliding (surface to surface) in ABAQUS.

³ Dilation angle used in ABAQUS is denoted β which can be found from the expression: $\tan(\beta) = \sin(\phi)$ where ϕ is the basic friction angle.

PRECEDING WORK

For further descriptions see Eltervaag (2012). The loading and geometry of the models are shown in figure 2.8.

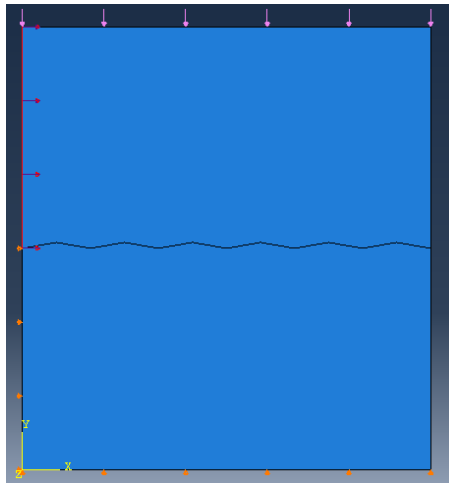


Figure 2.8: Loading of the models.

The results of the analyses compared to the actual tests are shown in figure 2.9 and 2.10 below.

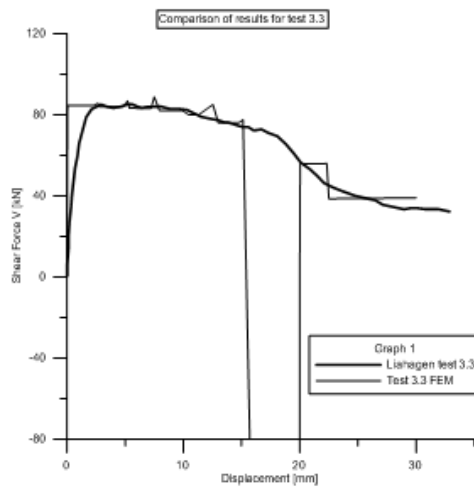


Figure 2.9: Comparison of FEM results and test results for test 3.3.

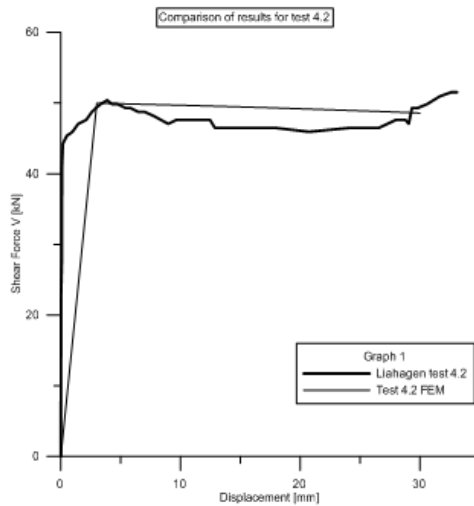


Figure 2.10: Comparison of FEM results and test results for test 4.2.

As previously mentioned the goal for these analyses was to evaluate whether FE-analyses could be used to assess sliding stability for concrete dams. The results presented in the figures above left the author optimistic regarding the usability of FE-analyses.

However, as shown in the figures the representation is not exact. It is believed that the “dip” in the numerical results shown in figure 2.8 is due to the prescribed displacement used to impose the horizontal force. When the upper part reaches the top of the asperities, the top part will slide down on the other side. The prescribed displacement now holds the upper part back from this movement, thus the reactions become negative. For further details see Eltervaag (2012).

Another issue with the models from the project is the material representation, and finding a better material model for rock and concrete is needed to obtain trustworthy results from FE-analyses. Developing more representative numerical models for sliding stability is the scope for this Master’s Thesis.

3. THEORY

This chapter presents the theoretical background for sliding failure mechanisms for concrete dams. The chapter is based on the literature study conducted in the author's Project work, and contains selected topics which describe the mechanisms for sliding failure. For the sake of report structure, it has been emphasized only to present literature which is directly relevant for the analyses conducted in this Thesis. However, some peripheral formulations are also given. The reason for this is that several established stability assessment methods are of empiric nature, and even though they are not directly used in this Thesis, they provide a foundation for comparison.

For a further description of both the presented formulations and further theoretical foundations, see Eltervaag (2012).

3.1 Assessing stability towards sliding

According to Norwegian rules and regulations stability regarding sliding for concrete dams must be verified along several possible sliding planes both in the dam and in the foundation (NVE 2005). The sliding stability of such a plane can be described in different ways (see APPENDIX A) but the principles are the same. In Norway the shear friction method is used, where the stability is expressed by a factor of safety (FS). For a horizontal sliding plane this factor is found from the following equation (NVE 2005).

$$FS = \frac{c \cdot A + \sum V \cdot \tan \phi}{\sum H} \quad (3.1)$$

Where c is a cohesive parameter, A is the plane's area, V and H are the vertical and horizontal forces subjected on the plane respectively. The frictional behavior of the plane's surfaces is expressed by $\tan(\phi)$. In other words, the factor of safety is calculated from the *averaged* normal stress and shear capacity of the sliding plane.

3.1.1 Shear capacity and failure mechanisms

The shear friction method is based on the Mohr-Coulomb criterion for describing the shear capacity of the sliding plane. This criterion states that the shear capacity, τ , is linearly dependent on the applied normal force, σ , through a material specific frictional parameter $\tan(\phi)$ plus a cohesive parameter, c . This can be expressed as follows (Johansson 2009).

$$\tau = c + \sigma \cdot \tan \phi \quad (3.2)$$

Note that in the formulations for shear capacity compressive normal stresses are positive, and eventual tensile stresses have negative sign. Today it is generally accepted that the shear capacity for non-continuous brittle materials is not sufficiently described by the Mohr-Coulomb criteria (Johansson 2009), however the criteria is still in use much due to its simple formulation.

In the 1960's it was recognized that the failure envelope for rock mass (rocks with joints and faults) was curved. One of the major contributions to this understanding was when Patton (1966) derived a bi-linear failure criterion from experiments with "saw-toothed" rock specimens shown in Figure 3.1. Patton observed that sliding occurred at lower levels of normal stress than what was needed to cut off the saw-toothed geometry. This failure mechanism can be described on the form:

$$\tau = \sigma \cdot \tan(\phi_b + i) \quad (3.3)$$

Where ϕ_b is the material specific friction angle (simply denoted ϕ in the Mohr-Coulomb relation) and i is the angle of the saw-teeth, called the asperity inclination or dilation angle.

When the normal stress exceeded a certain value the saw teeth were cut off at their base. Patton (1966) explained this as a change of governing failure mode, from a sliding failure along the material interface, to a failure in the material itself. The shear capacity regarding this material failure is described by:

$$\tau = c_x + \sigma \cdot \tan(\phi_r) \quad (3.4)$$

THEORY

Where c_x is the bond of the failing material, and ϕ_r is the residual friction angle of the failure plane. The shear envelope obtained from these expressions is shown in Figure 3.1 below.

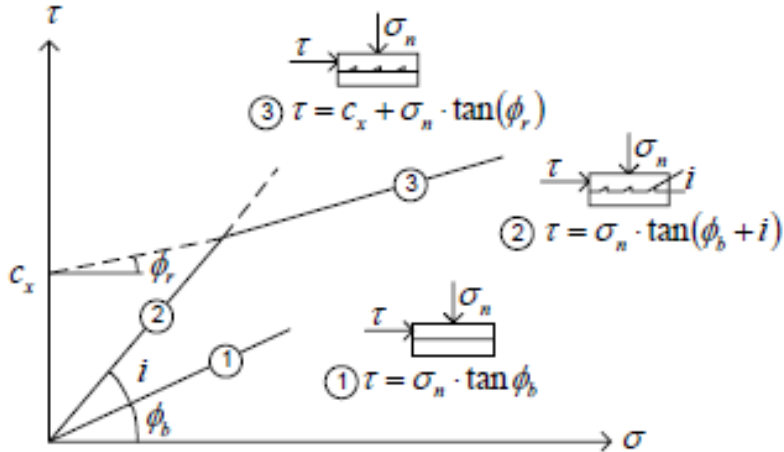


Figure 3.1: Patton's bi-linear failure criterion (Johansson 2009).

As seen in Figure 3.1 the relation first described by Mohr and Coulomb is still valid as long as the sliding plane is subjected to relative high (compressive) normal stresses. In other words, the shear capacity of the sliding plane when the asperities are cut off can be described by applying the frictional and cohesive parameters of the failing material to Mohr-Coulomb's criterion.

According to Patton (1966) the bi-linear failure envelope illustrates that there are two possible failure mechanisms for the rock specimens he studied. The first mechanism is sliding over the asperities (saw-teeth), and occurs at low normal stresses. The second is shearing through the asperities, and occurs at relatively high normal stresses. The bend in the failure envelope shown in Figure 3.1 is caused not by a switch of failure mode, but due to a change of ratio between the two failure modes occurring simultaneously (Patton 1966).

These different failure modes have also been described by Fredrik Johansson. In his Doctorial Thesis (Johansson 2009) he developed a conceptual model to describe sliding failure along rough unfilled rock joints. The model describes the sliding failure for one idealized asperity, and is then transformed to describe the failure along a full sized joint.

In the model for the idealized asperity Johansson (2009) identifies three failure modes, sliding along the side of the asperity facing the load, shear-failure along the base of the asperity, and tensile failure in the rock-base of the asperity. A sketch of an idealized asperity is shown in figure 3.2

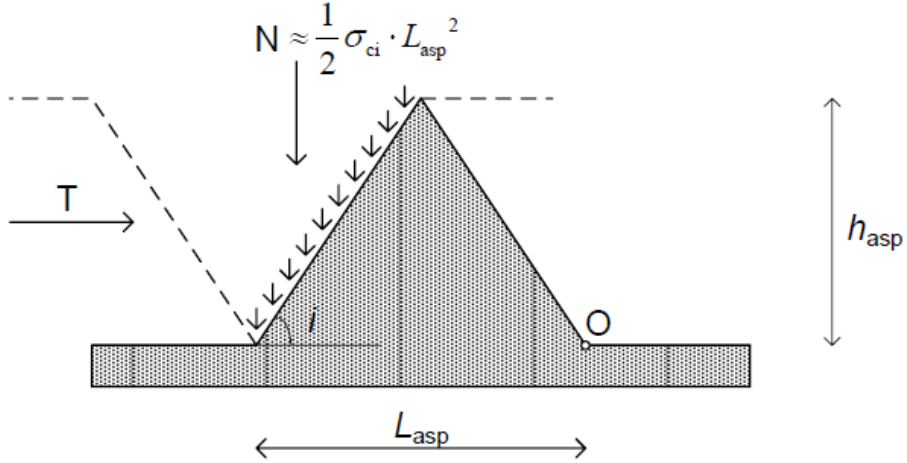


Figure 3.2: Principle sketch of an idealized 2D asperity (Johansson 2009).

To describe sliding along the loaded face of the asperity (the left side in Figure 3.2) Johansson uses Patton's formulation for shear capacity for low normal stresses (transformed from stresses to forces).

$$T = N \cdot \tan(\phi_b + i) \quad (3.5)$$

For a shear failure along the base of the material the equations for material failure (Mohr-Coulomb and Patton's equation for high normal stress) is used.

$$T = c_i \cdot L_{sp}^2 + N \cdot \tan(\phi_i) \quad (3.6)$$

For a tensile failure to occur in the rock-base, the vertical tensile stresses must exceed the tensile capacity of the rock. To calculate the average tensile stress in the rock, Johansson assesses the moment-equilibrium about point *O* in Figure 3.2.

$$T = \frac{(3 \cdot \sigma_{ci} + 4\sigma_{ti}) \cdot L_{asp}^2}{2 \cdot \tan(i)} \quad (3.7)$$

To illustrate these failure modes Johansson calculated an example for granite rock. Input values were as follows: uniaxial compressive strength: $\sigma_{ci} = 150$ MPa, tensile strength: $\sigma_{ti} = 10$ MPa, $c_i = 20$ MPa, $\varphi_i = 60^\circ$, $\varphi_b = 30^\circ$ and the basic length L_{asp} is set to 10 millimeters. The results are shown in Figure 3.3.

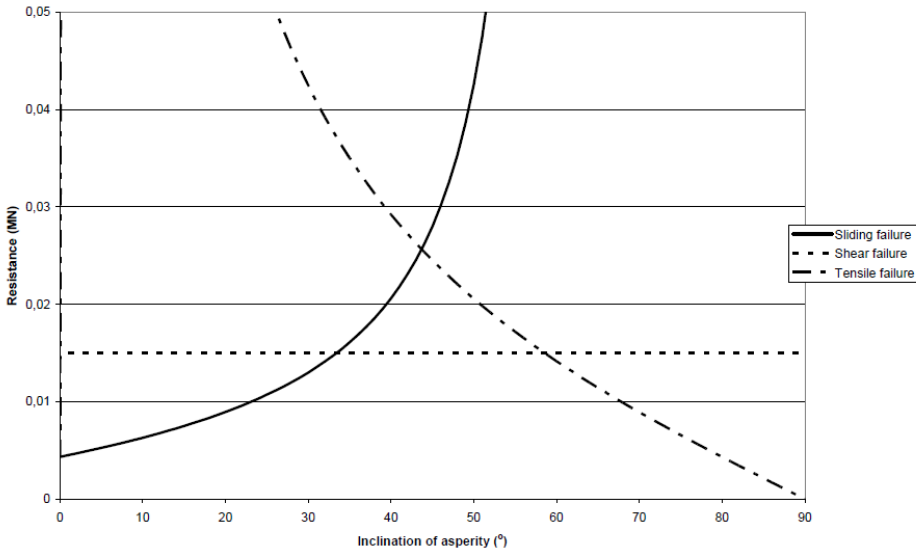


Figure 3.3: Different failure modes for an idealized asperity (Johansson 2009).

Based on the example over it appears that the maximum asperity angle in order to get sliding failure is 35° , and that tensile failure requires an asperity angle of 60° . It must be noted that both Johansson’s and Patton’s equation for sliding failure along asperities assumes no bond along the sliding surface.

The results shown in figure 3.3 indicate that not only the normal stress affect the failure mechanism, but also the inclination of the asperities. This means that for a granite asperity with an inclination of 40° , the failure is most likely governed by shearing even for relatively low normal stresses.

3.1.2 New methods for assessing stability towards sliding

Today, only the Mohr-Coulomb criterion is included in the stability calculations in Norway. In other words the contribution from surface roughness is overlooked. However, a new set of guidelines have been proposed in Sweden (Johansson et. Al 2012) which aims to present a more realistic assessment of the stability towards sliding.

These new guidelines include the two different failure modes of sliding along the surface and shearing off the surface roughness in the calculation of shear capacity. This is done by applying the Mohr-Coulomb criterion for sliding as a result of material failure, and including the dilation angle for sliding along an interface. The equations in the proposed guideline were originally presented as relations between shear and normal *forces*, which are in line with the current stability calculation methods. As seen in the previous section the shear capacity on the other side, is generally given as *stress*- relations. For the sake of consistency the equations in the new proposed guidelines also will be presented on stress-form.

The Authors identify three types of potential failure planes to be assessed: sliding along the dam-foundation interface, sliding along existing joints in the rock foundation and sliding as a result of failure in the rock mass.

Sliding along the dam-foundation interface is called failure type A. The failure along this sliding-plane can be calculated in two ways, depending on whether the interface is bonded or not. For failure without bond (Type A1) the shear capacity can be calculated as:

$$\tau = \sigma \cdot \tan(\phi_b + i) \quad (3.8)$$

For an interface which is completely or partially bonded the shear capacity is only calculated from the part of the surface with actual bond. The failure shear capacity (Type A2) can be calculated as:

$$\tau = c_a + \sigma_a \cdot \tan(\phi_b) \quad (3.9)$$

Where the subscript, *a*, denotes that only the cohesive parameter and normal force for the bonded part of the interface should be used. The proposed guideline emphasizes that the contribution from bonded and un-bonded parts

THEORY

of the interface not can be added together. The reason for this is that a bonded interface will have much higher resistance towards lateral displacements compared to an un-bonded interface (Johansson et al 2012).

For a sliding failure along an existing rock joint in the foundation (Type B) the guideline suggest that the shear capacity should be calculated as for interfaces without bond.

$$\tau = \sigma \cdot \tan(\phi_{bj} + i_j) \quad (3.10)$$

However, the basic friction and dilation angle governing this failure mode is connected to the rock joint. Thus the subscript, j , is introduced.

For a sliding failure as a result of a material failure in the rock mass (Type C) the capacity is found similar as for bounded interfaces.

$$\tau = c_r + \sigma \cdot \tan(\phi_r) \quad (3.11)$$

For this failure mode the cohesive and frictional parameters are related to the rock which is indicated by the subscript, r .

Johansson et. Al (2012) suggest that for the rock-concrete interface, the dilation angle can be found from field-measures of the larger asperities. If this is not possible they suggest studying pictures from the construction time. For dilation angles of joints in the rock mass field-measures of large scale asperities is suggested.

3.2 Alternative formulations

Another great contributor to the understanding of the shear capacity in rock mass is Nick Barton. Through his work (Barton 1973, Barton and Choubey 1977 and Barton and Bandis 1982) empirical formulations for the dilation angle of rock joints were established.

The major advantage with this approach is that the dilation angle can be found from a sample of the rock foundation. This is beneficial if the foundation geometry either is unknown or highly schistose with no clear failure plane. The dilation angle can be found as

$$i = JRC \cdot \log_{10} \left(\frac{JCS}{\sigma_n'} \right) \quad (3.12)$$

Where σ_n' is the applied normal stress, JRC is the Joint Roughness Coefficient (presented in tables) and JCS is the joint wall compressive strength.

Another benefit with the empirical approach is that scale effects on the surface roughness can be assessed. In short these effects are caused by how well the interface is mated, especially how well the smaller asperities are aligned. A small sample will have the necessary degree of freedom to rotate slightly, which can result in a better mated interface than what is found from samples at larger scales (Bandis et. Al 1981). The scale effects are presented more thoroughly in the authors project (Eltervaag 2012).

Through experimental work Fishman (2007, 2008 and 2009) launched a hypothesis of a new failure mode for concrete dams, called the Limit Turning Mode. Through his experiments Fishman found that failure of a concrete dam would happen over three stages. At stage one cracks will form at the upstream end of the dam. Due to continued horizontal loading these cracks will grow, and the compressive zone at the downstream end of the dam increases. At stage two the stresses in this zone has reached the material strength of the foundation and the rock is crushed. If the loading continues the crushed zone and the cracks will meet forming a continuous joint in the foundation. The dam has now reached stage three and is free to rotate independently of the rock foundation.

4. PRELIMINARY ANALYSES

In this chapter Liahagens tests are analyzed. These analyses serve two purposes. The primary objective is to get a better understanding of how the sliding failure develops, and what failure mode that governs the shear capacity. This enables a more correct description of the actual failure, which in turn provides better input parameters for numerical analyses of sliding failure.

Initially an approach was attempted where the basic friction angle was taken as the average from the tests. However, this method gave poor results. Thus a more profound analysis of the tests is conducted to obtain better values for the properties governing sliding failure. The test results are compared to the failure criteria described in chapter 3 to get an impression of how well the theory matches the tests. This comparison presents new insight in the development of failure, and provides more accurate values for the parameters governing the shear capacity of the sliding plane.

4.1 Finding the basic friction angle form test 4.2

Test 4.2 was the only test with a flat horizontal interface and no bonding between rock and concrete. This test was loaded with a normal force of 67.23 kN, and experienced a horizontal displacement of 33.23 mm. The load-displacement curves for both normal and shear forces are shown in figure 4.1.

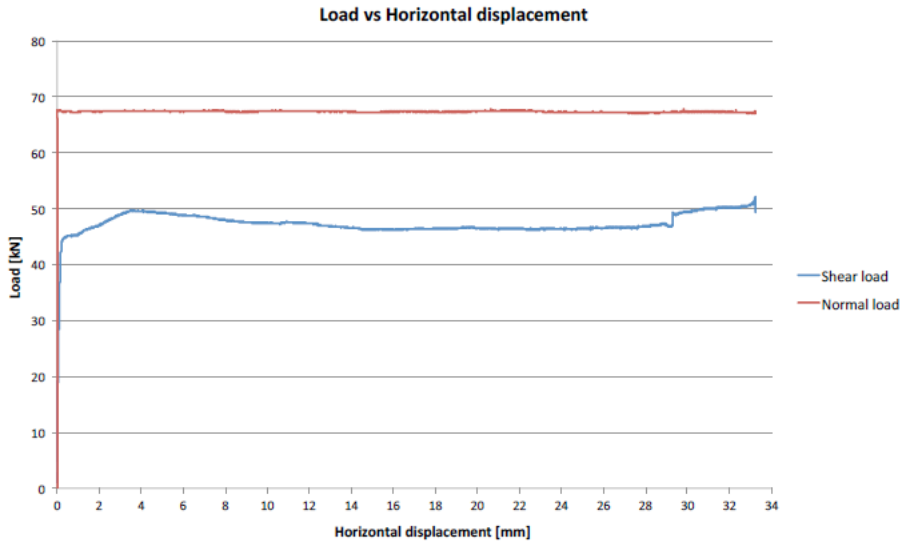


Figure 4.1: Load - displacement relations for test 4.2 (Liahagen 2012).

The test shows peak shear capacity of 52.04 kN at approximately 33 mm of displacement. This is not in line with the other tests, where the peak shear capacity is reached after only a few millimeters of displacement. From Liahagens Thesis no explanation of this irregular behavior is found, and this “peak” is therefore disregarded in these analyses.

Liahagen investigated the rock and concrete samples after the test and described a significant wear of the contact surfaces. This indicates that the reduction of shear capacity from five to fifteen millimeters of displacement might be explained as cut-off of micro roughness along the interface.

Assuming that the micro roughness is similar for all of the samples, the basic friction angle can be found from applying the Mohr-Coulomb criterion with zero cohesion to the forces at about four mm of displacement. Since the area is equal for normal and shear stresses this can be calculated directly from the forces:

$$\tan(\phi_b) = \frac{V}{N} \rightarrow \phi_b = \tan^{-1}\left(\frac{V}{N}\right) = \tan^{-1}\left(\frac{49.56}{67.23}\right) = 36.397^\circ \quad (4.1)$$

PRELIMINARY ANALYSES

A basic friction angle of 36.397° is somewhat lower than the expected value of 45° which is used by NVE (2005) and found in tables for granite (Barton and Chowbey 1977). A possible explanation for this might be that the preparation of the rock sample gives a smoother surface compared to natural rocks. The basic friction angle is believed to be material specific (Patton 1966, Johansson 2009) and is included in both the Mohr-Coulomb criteria as well as in Patton's equations.

After the micro roughness is cut off, the shear capacity is reduced. From the curves this residual shear capacity is found to be approximately 46 kN. Following the assumption that the micro roughness is similar for all of the samples the residual friction angle is found similarly to the basic friction angle. This gives a residual friction angle of 34.38° .

The effect of micro roughness cut-off might be evaluated through equation 3.6, which essentially is the Mohr-Coulomb criterion. In this way, the micro roughness is represented by a cohesive parameter. The friction angle to be used in this calculation must be the residual one, as this was found from the test after the "cohesion" was broken.

$$V = c \cdot A + N \cdot \tan(\phi_{residual}) \rightarrow c = \frac{V - N \cdot \tan(\phi_{residual})}{A} \quad (4.2)$$

Inserting values for the maximum shear capacity, 49.56 kN, normal force, 67.23 kN, and joint area (240 by 240 mm which equals 0.0576 m^2) this cohesive parameter is found to be 62 kPa.

The results also show a gradual build-up of shear capacity, which indicates that the samples might slide a certain distance before shearing of the micro roughness starts. One explanation for this can be that the samples contained grooves with length in the sliding direction of up to 5 mm. In this way the micro roughness could have been moving within these grooves without contributing to the shear capacity. However, for this to be the case a similar behavior should be seen in the other tests as well, which in general is not found. Thus, a more probable explanation for this effect is errors in the test setup and/or calibration of the monitors used for this actual test.

4.2 Failure of test series 3

Test 3.1, 3.2 and 3.3 (hereafter referred to as test series 3) has an interface asperity-inclination of ten degrees. The load-displacement curves for these tests are shown in figure 4.2 below. In this test series only test 3.1 shows a gradual increase of shear capacity.

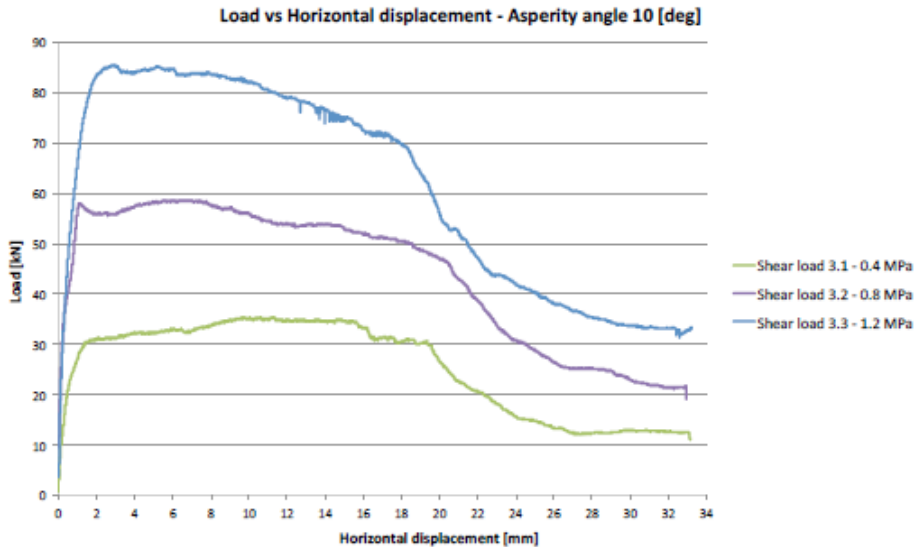


Figure 4.2: Load-displacement relations for test series 3 (Liahagen 2012).

Studying pictures of the tests (see APPENDIX B) it appears that the failure mode for these tests is sliding over the asperities. According to the theory, the peak shear capacity for this failure mode is best described by applying the basic friction angle to Patton's equation (equation 3.3). In table 4.1 this criterion is compared to the actual tests and the Mohr-Coulomb criterion used in today's guidelines.

Table 4.1: Comparison of peak shear capacity for test series 3.

Sample	From Liahagen			Mohr-Coulomb		Patton	
	i [°]	N [kN]	V [kN]	V [kN]	Error [%]	V [kN]	Error [%]
3.1	10	24.82	35.38	18.29	48	26.06	26
3.2	10	45.98	58.70	33.89	42	48.28	18
3.3	10	67.65	85.43	49.86	42	71.04	17

PRELIMINARY ANALYSES

The error is found as the difference between the calculated shear force and the exact shear force observed by Liahagen.

$$Error = \left| \frac{V_{calculated} - V_{exact}}{V_{exact}} \right| \cdot 100 [\%] \quad (4.3)$$

These results show that even though the peak shear force obtained from Patton's equation does not match the observed one from Liahagen, it improves the accuracy significantly compared to using the Mohr-Coulomb criterion.

All these tests show a decline in shear capacity after the initial failure, even though the normal force actually increased somewhat (approximately 5 kN) as the samples moved up the asperities. This decline is as for test 4.2 described as micro roughness cut-off.

At 20 mm of displacement the samples slides over the asperities and the normal force changes from a stabilizing to a driving force. Hence the residual shear capacity is found at approximately 18 mm of displacement in figure 4.2. In the table below the residual capacity for test series are compared to Patton's equation using the residual friction angle instead of the basic friction angle. In table 4.2 the normal force applied in the tests have been increased according to the actual test.

Table 4.2: Comparison of residual shear capacity for test series 3.

Sample	From Liahagen			Patton	
	i [°]	N [kN]	V [kN]	V [kN]	Error [%]
3.1	10	27.7	30.6	27.1	11
3.2	10	49.2	50.4	48.1	4.5
3.3	10	71.3	69.7	69.8	0.1

The results from Patton's equation fits better for residual shear capacity compared to the peak capacity. The reason for this might be that the initial micro roughness has greater variance from sample to sample than anticipated. When the micro roughness is cut-off this variance is excluded.

As for test 4.2 the cutting of micro roughness might be described by equation 3.6. However, for these tests the baseline of the micro roughness is not horizontal but inclined to the angle of the asperities.

The gross shear capacity can then be assessed by the shear friction method for inclined sliding planes which is given in the Norwegian guidelines (see APPENDIX A)

$$FS = \frac{\frac{c \cdot A}{\cos \alpha (1 - \tan \alpha \cdot \tan \phi)} + \sum V \cdot \tan(\alpha + \phi)}{\sum H} \quad (4.4)$$

However, the inclination of the sliding plane which in the above equation is denoted α is identical to the inclination angle of the asperities, i . Also, when assessing the shear capacity the factor of safety, FS , can be set to 1.0. Thus the following equation for peak shear capacity is obtained:

$$V = \frac{c \cdot A}{\cos i (1 - \tan i \cdot \tan \phi_{residual})} + N \cdot \tan(\phi_{residual} + i) \quad (4.5)$$

The cohesive parameter, c , is only active on the front side of the asperities. Thus, the area, A , is only half of the total interface. From the geometry in figure 2.7 this area is found to be 29 238 mm² for test series 3. Applying the values for initial shear force, V , initial normal force, N , residual friction angle and inclination angle from Liahagens test the cohesive parameters in table 4.3 are found.

Table 4.3: Cohesive values for micro roughness for test series 3.

Test	Cohesion [kPa]
3.1	309
3.2	382
3.3	536

The cohesive parameters presented in the table above can be seen as the varying micro roughness among the tests. Compared to test 4.2 these values are much higher. An explanation for this might be that due to the interface geometry the contact area is much smaller, resulting in increased wear. It

PRELIMINARY ANALYSES

should also be noted that the cohesive parameters increase for increasing normal forces. As argued by Patton in section 3.1.1 of this Thesis, one reason for this might be that for the actual failure of the samples with low normal forces, more sliding over than shearing off the micro roughness occurs. For the tests with high normal force the failure will be totally dominated by shearing.

As shown in figure 3.3 the shear resistance for roughness cut-off is equal for all asperity angles, while for sliding failure it increases with increasing angles. This indicates that for an interface with varying asperity angles, the steeper ones will be cut off while the ones with lower inclination will slide. The more shearing failure to occur, the higher the total shear capacity of the interface will be. The result of this is that the cohesive parameter for describing the shearing will increase with higher normal stress.

4.3 Failure of test series 2

Test series 2 consists of test 2.1, 2.2 and 2.3. Also for these tests the normal force increased as the samples were displaced horizontally. The load displacement relationship is presented in figure 4.3.

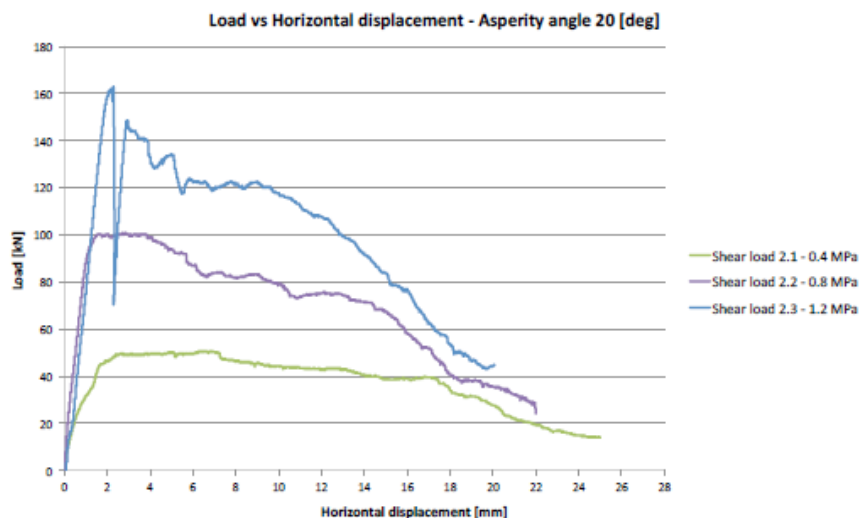


Figure 4.3: Load-displacement relations for test series 2 (Liahagen 2012).

As seen in figure 4.3 above also this test series exhibits decrease in shear capacity for further displacement after peak capacity. From the pictures in APPENDIX B it is found that for these tests the peak capacity is reached for sliding prior to cutting off the asperities. The residual capacity is governed by sliding over these cut off asperities.

This shearing of asperities is somewhat surprising compared to the results from Johansson in figure 3.3 where shearing failure did not govern the sliding failure for inclinations below 35°. However, the input values in that calculation was chosen to represent sliding of two samples of granite (Johansson 2007). From USBR (1977) the cohesive parameter of intact concrete is given as ten percent of the compressive strength, and the internal friction angle is suggested to be 45°. From Liahagen (2012) the compressive strength of the concrete used in the tests is found to be 58 MPa.

Applying these values to equation 3.5 and 3.6, and updating the normal force and residual friction angle to match test series two, the diagram in figure 4.4 is obtained for the shear capacity for one single asperity in Liahagens tests.

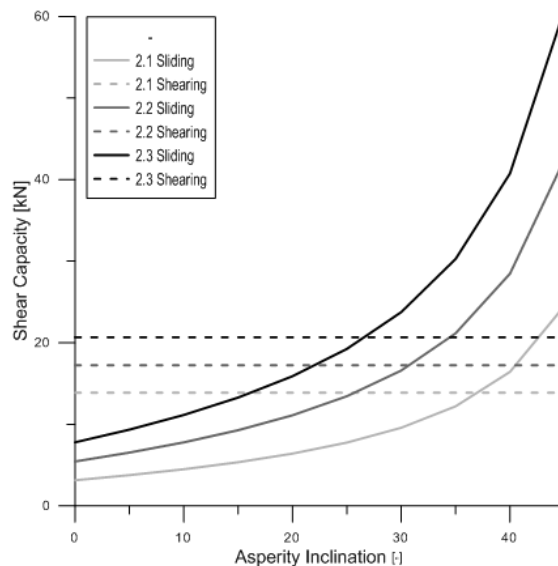


Figure 4.4: Sliding and shearing failure capacity for test series two.

PRELIMINARY ANALYSES

From the figure above it is seen that the governing failure mode is influenced both by the normal force and the inclination angle of the asperities. Unfortunately these calculations cannot describe the partly shearing of the asperities which is seen in this test series, but it gives an indication that the larger the normal force, the more likely a shearing failure becomes. It should also be mentioned that the shear parameters are given very coarsely in USBR (1977) so these calculations should be seen as indications rather than exact predictions.

As for test series 3 the theoretical peak shear capacity found from Patton's equation and the Mohr-Coulomb criterion has been compared to the actual test results in table 4.4.

Table 4.4: Comparison of peak shear capacity for test series 2.

Sample	From Liahagen			Mohr-Coulomb		Patton	
	i [°]	N [kN]	V [kN]	V [kN]	Error [%]	V [kN]	Error [%]
2.1	20	27.57	50.74	20.32	59	41.49	18
2.2	20	47.77	100.59	35.21	65	71.89	28
2.3	20	68.36	162.83	50.39	69	102.88	37

Also for test series 2 the results are improved by including the asperity angle in the calculations, however the error is larger compared to test series three.

In order to compare how well the theory fits for the residual capacity, the actual inclination angle after the asperities have been cut must be estimated. The asperities are cut with great variation, and it is hard to find exact values for the final asperity angle from the pictures. It is assumed that for test 2.1 the total asperity angle is reduced by approximately 5°, for test 2.2 the reduction is around 10°, and for test 2.3 the residual sliding plane is close to horizontal. The increase in the normal force is included in the comparison shown in table 4.5 below. The forces are found for 17 mm displacement for test 2.1 due to some shearing which appears to have reduced the tip of the asperities so that sliding over occurred somewhat prior to 20 mm. For test 2.2 and 2.3 the values have been found from 20 mm of displacement.

Table 4.5: Comparison of residual shear capacity for test series 2.

Sample	From Liahagen			Patton	
	i [°]	N [kN]	V [kN]	V [kN]	Error [%]
2.1	15	33.6	39.5	39.2	0.7
2.2	10	55.5	35.4	54.3	53
2.3	0	74.34	44.37	50.9	31

The table above indicates that this way of assessing the shear capacity gives large errors when the interface degradation exceeds a few degrees. When the asperities of the interface deforms the continued sliding follows a new and smother sliding plane. The new sliding plane is so decomposed that the residual friction angle might differ significantly from the one calculated from test 4.2. This combined with the insecurity in residual inclination angle are believed to be the source of the errors presented in table 4.5.

Also for this test series, the effect of the cutting of asperities can be estimated trough equation 4.4, but due to the poor confidence in the residual values, large errors are to be expected. The cohesive values from this calculation is based on an intact interface where only the side facing the displacement ($A = 0.03066\text{m}^2$) contributes to the shear capacity. The results are presented in table 4.6.

Table 4.6: Cohesive values for micro roughness for test series 2.

Test	Cohesion [kPa]
2.1	282
2.2	781
2.3	1552

4.4 Failure of test series 1

The load displacement relationship of test 1.1, 1.2 and 1.4 are shown in figure 4.5 below.

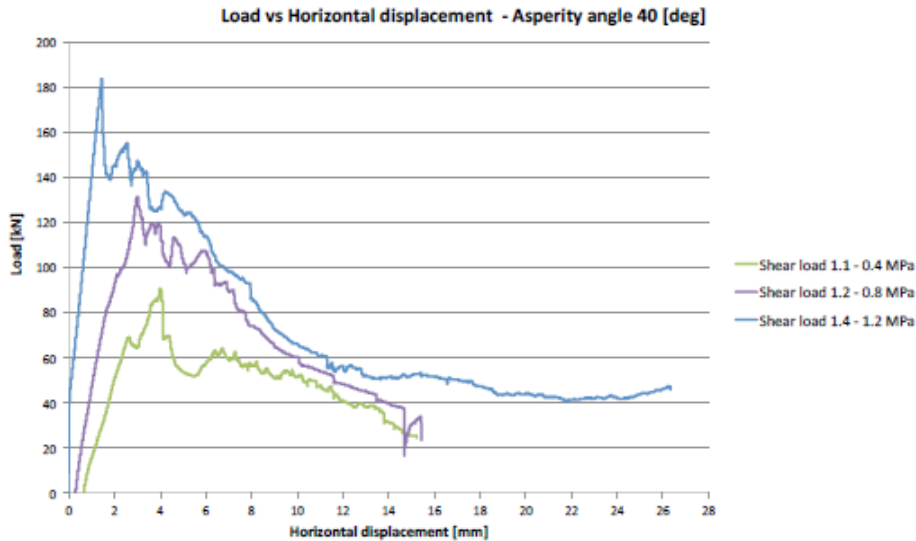


Figure 4.5: Load-displacement relations for test series 1 (Liahagen 2012).

From the pictures it appears that the governing failure mode for these tests are shearing off the asperities. The peak shear capacity can then be found from equation 3.6, which describes cutting off the asperities. The pictures show that the concrete asperities fail prior to the rock. Thus the shear capacity of the concrete governs the failure.

As for the other test series the results from calculations based on the Mohr-Coulomb criterion and Patton's equation have been compared. However for this test series the Mohr-Coulomb criterion are presented for material failure in the concrete alone, while Patton's equation is used to assess sliding over the initial asperities. From the pictures it is found that the asperities are cut off close to their base, so the residual sliding plane becomes approximately horizontal. Thus the area, A , for cohesive contribution to the shear capacity of the concrete material becomes 240 mm x 240 mm, which leads to a cohesive contribution of 334.08 kN for this test series. The comparison is shown in table 4.7 below.

Table 4.7: Comparison of peak shear capacity for test series 1.

Sample	From Liahagen			Mohr-Coulomb		Patton	
	i [°]	N [kN]	V [kN]	V [kN]	Error [%]	V [kN]	Error [%]
1.1	40	27.52	90.53	361.60	332	113.73	26
1.2	40	46.91	131.19	380.99	190	193.86	48
1.4	40	68.49	183.42	402.57	119	283.04	54

The table above show that neither the Mohr-coulomb criterion nor Patton’s equation are able to describe the failure for these tests. However, the input values for the Mohr-Coulomb criterion appears to be given rather approximately. For instance the USBR lists the cohesive parameter as “*about ten percent of the compressive strength*”. Thus, more realistic results might be obtained by treating the shearing of the asperities in the same way as for shearing of micro roughness.

For this test series the residual sliding plane is horizontal, thus the shear capacity can be found as done for test 4.2. The cohesive parameters obtained from this calculation are presented in table 4.8.

Table 4.8: Cohesive values for macro roughness for test series 1.

Test	Cohesion [MPa]
1.1	1.24
1.2	1.72
1.3	2.37

As for test series three this method gives higher cohesive parameters for higher normal forces. For this calculation the basic residual friction angle from test 4.2 has been used. The relevance of this might be debated due to the distortion for the interface. This is discussed in section 6.1.4.

4.5 Failure of tests with bond

Liahagen conducted two tests with bond. Test 4.1H with horizontal interface and test 1.3H with 40° asperities. The load displacement relations for these tests are shown in figure 4.6. For these two tests the normal force was kept constant through the testing.

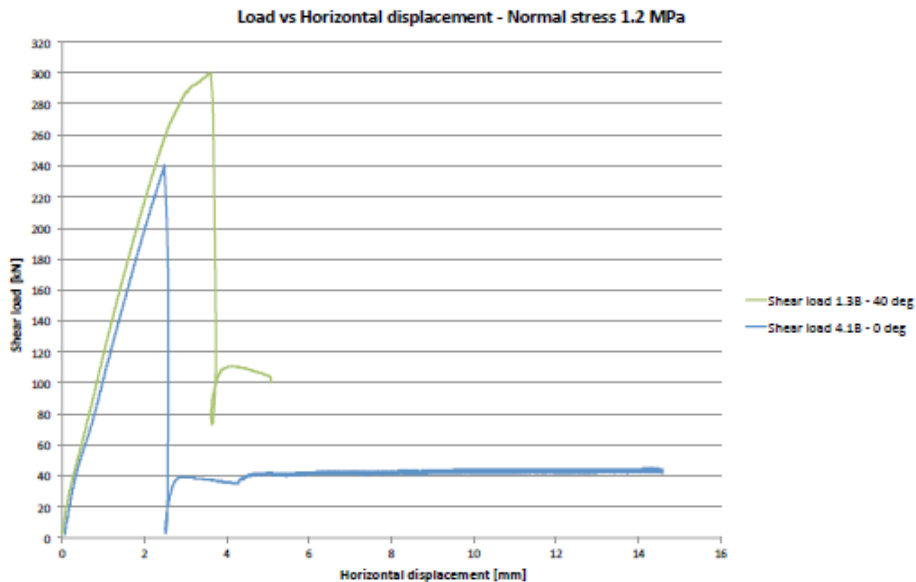


Figure 4.6: Load-displacement relation for test with bond (Liahagen 2012).

The failure of these tests is of a more brittle character compared to the tests without bond. The failure mechanism for these tests naturally fit the Mohr-Coulomb criteria. From the pictures it is found that test 4.1H cuts off the interface between rock and concrete and follows a horizontal sliding plane. For test 1.3H the failure plane is declined and goes from the rock to the concrete.

Values for the cohesive and friction parameters are hard to estimate since test 1.3H was stopped before stable readings of the residual capacity were achieved. However, the brittle characteristics of the failure suggest that the residual capacity for test 1.3H is in the range of the readings at about 5mm.

The drop in shear capacity as the bond fail coincides for the two tests and gives good estimate for the cohesion. The failure of the cohesion reduces the

capacity with 200 kN, which translates to a cohesive parameter of 3.47 MPa for the Mohr-Coulomb criteria. The friction angles can be found from the post-peak capacity, and equals approximately 30° for test 4.1H. For test 1.3H the residual capacity is assumed to be around 100 kN, and the friction angle about 54°.

However, due to the declined failure plane of test 1.3H the assumption of 100kN rest capacity could be too high. This in turn inflicts errors in the estimation for friction angle, which then also might be too high. The Author remains suspicious of the estimates for test 1.3H since the data from the test are highly deficient.

4.6 Discussion

The results found in this chapter are summarized in table 4.9 below:

Table 4.9: Results from hand calculations.

Sample	Inclination [°]	Failure mode		Cohesion [kPa]	Residual inclination [°]
		Peak	Residual		
1.1	40	Shearing	Shearing	1245	0
1.2	40	“	“	1720	0
1.3H	40	“	Sliding	3470 ⁴	0
1.4	40	“	Shearing	2371	0
2.1	20	Sliding	“	282	15
2.2	20	“	“	781	10
2.3	20	“	“	1552	0
3.1	10	“	Sliding	309	10
3.2	10	“	“	382	10
3.3	10	“	“	536	10
4.1H	0	Shearing	“	3470 ⁵	0
4.2	0	Sliding	“	62	0

The test results show that for a bonded interface the shear capacity is not only dramatically higher compared to un-bonded interfaces, but also well described by the Mohr-Coulomb criterion used in today’s guidelines. Nevertheless, the

⁴ With basic friction angle of 54°

⁵ With basic friction angle of 30°

PRELIMINARY ANALYSES

Mohr Coulomb criterion shows an average error of 107%⁶ for un-bonded samples.

For un-bonded interfaces, it appears that the residual behavior is reasonably well described by applying the residual friction and inclination angles to Patton's equation (average error 17%). This fits the assumption of a material specific basic friction angle after the roughness is cut off.

The peak capacity is not so well described by applying the basic friction angle to Patton's equation (average error 27%). The reason for this is believed to be variations in micro roughness among the tests. However, the peak capacity is well described by applying the residual friction angle, and adding a cohesive parameter which takes the shearing of micro or macro roughness into account.

For test series 2 and 3 the Mohr-Coulomb and Patton criteria underestimate the capacity, while for test 1 they give too high values. This indicates that the simplified calculations not always will give conservative estimates.

Interestingly, even after the surface micro roughness is worn down the shear capacity is higher for the inclined interface of test 3.3 with equal normal load as test 4.2. In other words: the increase in residual shear capacity of test series 3 shows that only to consider the mean inclination of the sliding plane does not take the contribution from roughness sufficiently into account. For the tests where the interface is demolished this naturally depends on the residual inclination of the initial asperities.

Compared to figure 3.3 it appears that shearing trough the asperities happens for a lower asperity angle than 35°. For test series 2 with 20° asperity angle it appears to be a change in governing failure mode, at least for relatively high normal stresses. At 40° the shearing failure mode is completely dominating the shear capacity and the failure behavior.

The softening behavior succeeding the roughness cut-off is not described in any of the criteria, and will be hard to include in hand calculations. Including cohesive softening is possible in numerical models, which enables the analyst to model a progressive sliding failure development which is not captured trough the conventional hand calculations.

⁶ If test series 1 is excluded the average error is reduced to 54%.

5. NUMERICAL MODELS OF SLIDING STABILITY

Following the advice of co-supervisor Gabriel Sas, the finite element software ATENA has been used for the numerical models. ATENA is a software package developed by Cervenka Consulting, tailor-made for analyzing concrete structures containing sophisticated material models. For the work with this Thesis the version ATENA-Science has been used, which enables pre and post-processing in the software GiD developed by CIMNE International, Center for Numerical Methods in Engineering.

This chapter is subdivided into eight sections. The first seven present the stages in the modeling of Liahagen's tests, while the last section presents the modeling of dam Ipto.

To model contact in ATENA, special contact elements are required. The properties of these elements serve both as physical parameters but also as numerical tools in the analyses. Thus, the contact formulations are presented extensively.

5.1 Geometry

The tests from Liahagen were initially modeled in 3D with a width of 240 mm normal to the loaded direction. However, due to vast numerical problems with these analyses the strategy was changed to 2D plane stress models as in the project. The sliding/shearing failure is a two dimensional problem, so 2D models should be sufficient to represent the actual shear tests. The advantage with 2D models is that the number of elements is reduced which again reduce the computational time. This has been very beneficial for the troubleshooting.

The 2D tests have been given a steel frame to avoid numerical troubles when applying the loads directly to the concrete. The model of test 3.3 in GiD is shown in the figure below.

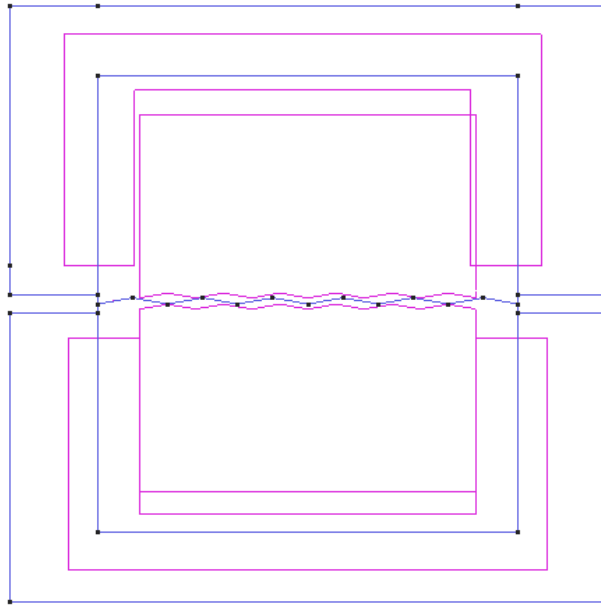


Figure 5.1: 2D geometrical model of test 3.3

The contact parameters were assigned to separate contact-volumes (3D) or surfaces (2D). The contact-volume only expands two dimensions and the contact surface only one. These geometrical features serve simply for assigning the contact boundary-conditions.

Due to numerical problems the analyses of test series one had to be modeled somewhat different than what was anticipated. For these tests the analyses with asperities crashed shortly after the concrete started to crack, and thus no failure history could be obtained. The failure of these models is presented further in section 6.1.4. To obtain a failing history, this test series is modeled with a flat interface and using the cohesive parameters from chapter four.

5.2 Modeling contact in ATENA

ATENA uses interface elements to model contact between two parts in a model. An interface in ATENA is defined by a pair of lines (surfaces for 3D analyses). These lines can either share the same position, or they can be separated by a gap. According to the ATENA users manual (Cervenka et. Al 2013) the interface can exist in two states:

- Open State: No interaction of the contact sides.
- Closed state: Full interaction of the contact sides. In this state friction sliding along the interface is possible, as long as the interface element(s) have been assigned a friction model.

To model the behavior of the interface elements ATENA uses the Penalty Method. For this purpose the following constitutive matrix of the interface is defined (Cervenka et. Al 2013)

$$\mathbf{F} = \begin{Bmatrix} F_\tau \\ F_\sigma \end{Bmatrix} = \begin{bmatrix} K_u & 0 \\ 0 & K_m \end{bmatrix} \begin{Bmatrix} \Delta u \\ \Delta v \end{Bmatrix} = \mathbf{D}\mathbf{u} \quad (5.1)$$

in which Δu and Δv are the relative displacements of the interface sides in the local coordinate system: r, s , aligned with the gap orientation (see figure 5.3). K_u and K_m are the shear and normal stiffness respectively. These coefficients can be regarded as the stiffness of one material layer having a finite thickness. In other words high values of K_u and K_m correspond to a high penalty-number (Cervenka et. Al 2012). F_τ and F_σ are forces at the interface again referred to the local coordinate system. The typical behavior for the interface material model in shear and tension is shown in figure 5.2 below.

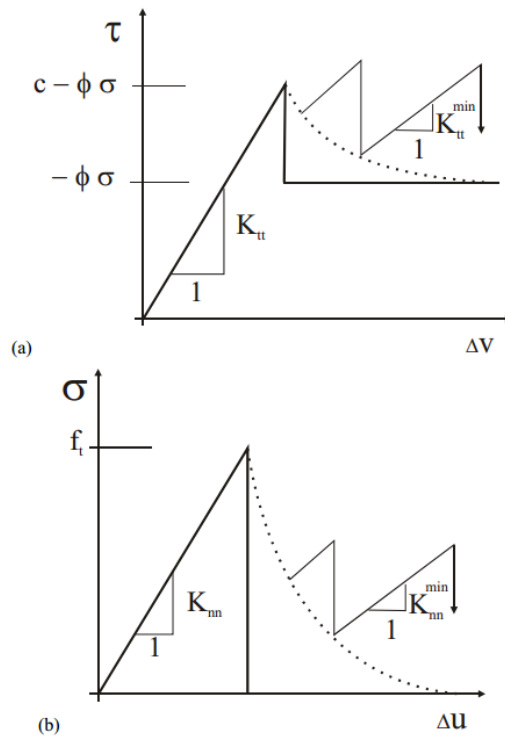


Figure 5.2: Typical interface behavior in shear and tension (Cervenka et. Al 2012).

There are two additional stiffness values, K_{nn}^{min} and K_{tt}^{min} , that needs to be specified for the Interface material. These values are only used for numerical purposes after the failure of the interface material. Theoretically, after the interface is broken its stiffness should be zero. However, this would lead to an indefinite global stiffness (Cervenka et. Al 2012). The ATENA theory manual (Cervenka et. Al 2012) recommends setting these values between 0.01 and 0.001 times the initial ones.

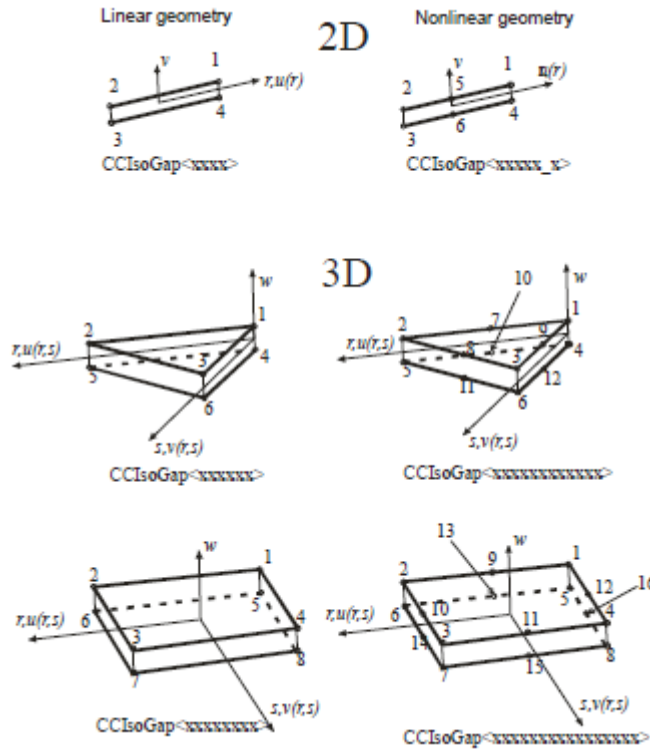


Figure 5.3: Sketch of interface elements in ATENA (Cervenka et. Al 2012).

Derivation of gap elements is presented here according to Cervenka et. Al (2012) for the linear 2D interface element `CCIsoGap<xxxx>` showed in figure 5.3. The element has two degrees of freedom (d.o.f) defined in r, s and relative displacements Δu and Δv are defined as follows

$$h_1 = \frac{1}{2}(1+r), \quad h_2 = \frac{1}{2}(1-r)$$

$$\Delta \mathbf{u} = \begin{bmatrix} \Delta u \\ \Delta v \end{bmatrix} = \begin{bmatrix} h_2 \Delta u_{1,4} + h_1 \Delta u_{2,3} \\ h_2 \Delta v_{1,4} + h_1 \Delta v_{2,3} \end{bmatrix}$$

$$\Delta \mathbf{u} = \begin{bmatrix} h_1 & 0 & h_2 & 0 & -h_2 & 0 & -h_1 & 0 \\ 0 & h_1 & 0 & h_2 & 0 & -h_2 & 0 & -h_1 \end{bmatrix} \begin{bmatrix} u_1 \\ v_1 \\ u_2 \\ v_2 \\ u_3 \\ v_3 \\ u_4 \\ v_4 \end{bmatrix} = \mathbf{B} \mathbf{u} \quad (5.2)$$

The rest of the derivation follows the same path as other elements, with stiffness $\mathbf{K} = \int \mathbf{B}^T \mathbf{D} \mathbf{B} dV$ and internal force-vector $\mathbf{Q} = \int \mathbf{B}^T \mathbf{F} dV$. The interface element stiffness-matrix, is integrated numerically in two Gauss points (Cervenka et al 2012). Both K and Q are established according to the local coordinate system. Thus, they must be transformed to global coordinates before they can be assembled in the problem's governing equations.

The stiffness is depending on the gap state. If the normal force F_σ exceeds the tensile strength of the interface R_{it} , the gap is considered open. The corresponding constitutive law, stress free interface, can be written as:

$$\begin{Bmatrix} F_\tau \\ F_\sigma \end{Bmatrix} = \begin{Bmatrix} 0 \\ 0 \end{Bmatrix} \quad (5.3)$$

The stiffness coefficients are set to small but nonzero values; K_{tt}^{op} and K_{mm}^{op} . If the normal force does not exceed the tensile strength, the gap is considered closed. For this situation the stiffness coefficients should be set to large values. According to Pryl (2013) the stiffness coefficients in the closed state should be chosen according to thickness-comparable neighbor quadrilateral elements. A good starting point is advised to be ten times the stiffness of the stiffest neighboring elements, i.e:

$$K_{nn} = K_{tt} = \frac{E_{neighbor}}{element\ size} \cdot 10 \quad (5.4)$$

For contact in open state the values can be chosen approximately 1000 times smaller (Pryl 2013).

The properties for the contact elements used in ATENA are governed through interface materials in GiD. An example of the material description used in this Thesis is shown in figure 5.4 below.

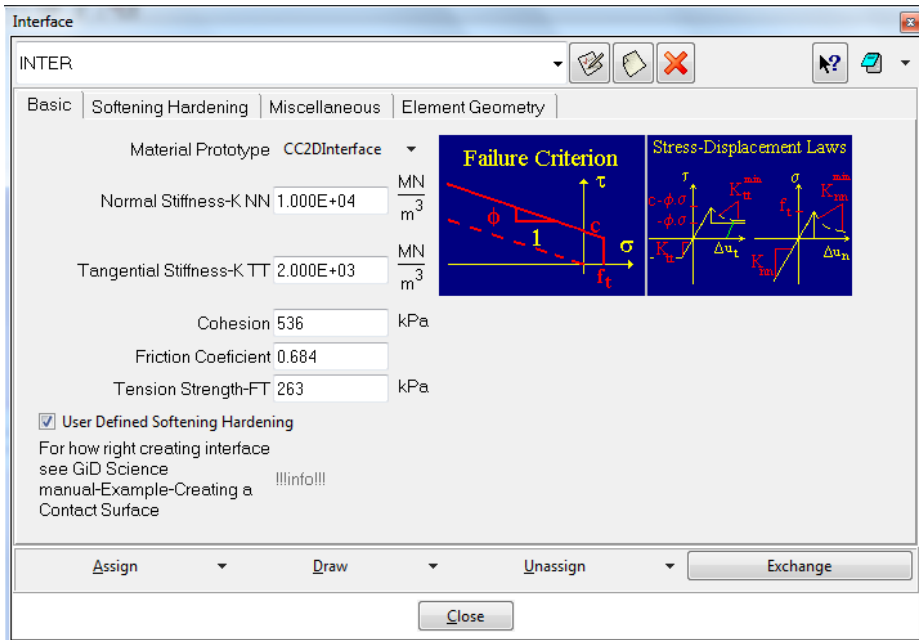


Figure 5.4: Material parameters for the Interface material for test 3.3 in GiD.

The material parameters are set according to the procedure described in chapter four. Thus, the friction parameter is equal for all the tests calculated as $\tan(\phi_{residual})$, and the cut-off of surface micro-roughness is included through a cohesive parameter. Pryl (2013) advises a relation where the value of the tensile strength, f_t , is set as half of the cohesive value in order to avoid numerical problems. For all the analyses run in this Thesis, these parameters are set according to this relation.

As previously mentioned, the modeling of concrete cut-off for test series one and two proved hard to model. For test series one the general approach has been to give the interface a large cohesive value, and then gradually decrease the concrete tensile strength and onset of crushing to get failure. However, by modeling this test series with a flat interface, and include the cut-off of the asperities trough a cohesive parameter, the sliding failure history has been obtained. The cohesive values used in the models are presented in table 5.2.

The interface material model enables a user specified softening behavior of the cohesive parameter. The softening parameters have been found for the individual tests by studying the original load-displacement graphs from Liahagen and are presented in APPENDIX D. The gradual increase of shear capacity prior to the micro roughness cut-off could be included trough the softening functions. However, since this behavior only is seen in test 3.1 and 4.2 it is assumed that it is caused by errors in the test setup and therefore disregarded.

5.3 The material models

As in the project both the concrete and rock have been modeled as concrete. The decision for modeling the rock as concrete is based on the behavior of the actual rock samples. Through discussions with co-supervisor Gabriel Sas and Dobromil Pryl at Cervenka Consulting it was decided that this behavior is more in line with the available material models for concrete than rock. As described in section 5.1, the models have been made with a steel frame which is modeled as an elastic material. The materials are shown in figure 5.5. Naturally the interface material with no expansion in the x-y plane is invisible, but it is located between the ROCK+ and the CONCRETE+ materials.

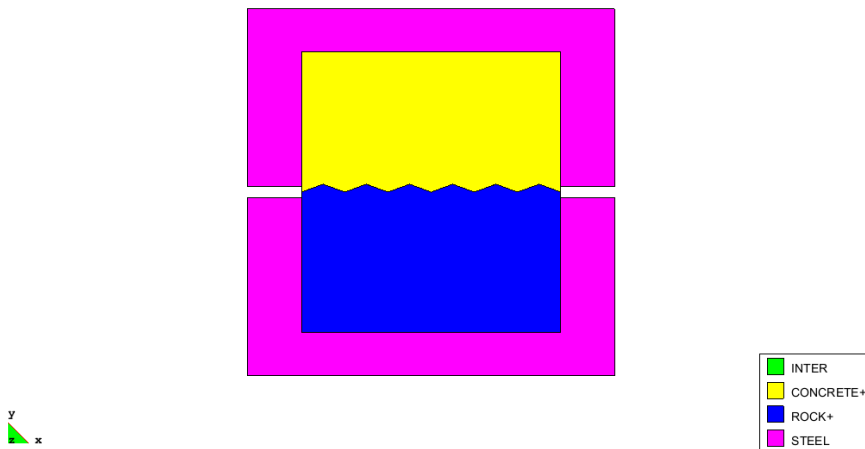


Figure 5.5: Illustration of the material allocation in GiD (test2.3).

5.3.1 The concrete material model

Concrete is a brittle material with significantly higher strength in compression than in tension. Under tensile loading cracks typically form normal to the load, while for compressive loading micro cracks develop in planes parallel to the load (Sas et. Al 2013). As shown in figure 5.6, the material exhibit hardening behavior after the elasticity limit for compression is reached. The material hardens with a decreasing slope of the stress-strain curve until the compressive strength is reached. After the compressive strength is reached the curve drops significantly and eventually crushing failure occurs at some ultimate strain (Sas et. Al 2013).

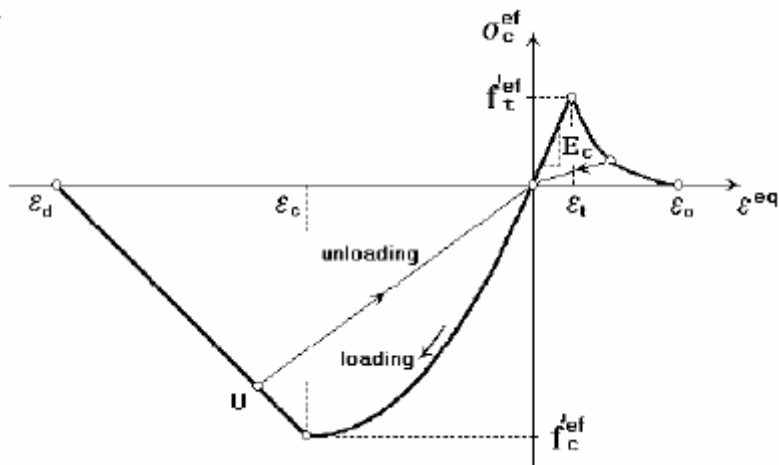


Figure 5.6: Uniaxial concrete behavior (Cervenka et. Al 2012).

Both rock and concrete is modeled with the Cementious2 material model in GiD. This model is based on the CCxDNonLinCementious material model in ATENA which is a fracture-plastic material model that combines constitutive models for both tensile and compressive behavior of concrete. The tensile, (fracture) behavior of concrete is based on the classical orthotropic smeared cracking formulation and crack band model (Cervenka et. Al 2012). The material model uses a Rankine failure criterion, exponential softening, and it can be used as a rotated or fixed crack model. The compressive behavior of concrete is described through a plasticity model for concrete crushing. This is a hardening/softening plasticity model based on the Menétrey-William failure surface. This model uses a return mapping algorithm for the integration of constitutive equations (Cervenka et. AL 2012).

The combined model is similar to multi surface plasticity, but in addition it enables modeling of physical changes such as crack closure. Also tensile and compressive strength reduction after crushing is included. For a more thorough description of the CCxDNonLinCementious material model see APPENDIX E.

The material parameters found in Liahagen (2012) were not sufficient to describe the materials in ATENA. Some additional values have been found from Eurocode 2 and Nilsen and Thidemann (1993), but not all that were needed. ATENA enables the user to model concrete according to the

NUMERICAL MODELS OF SLIDING STABILITY

Eurocode directly by just inputting the strength-class. This has provided default values for the missing parameters. The material parameters are listed in table 5.1 below.

Table 5.1: Material parameters for concrete material models

Material	Concrete	Rock
Young's Modulus [GPa]	37	100
Poisson's Ratio	0.2	0.2
Tensile strength [MPa]	4.1	0.733
Compressive Failure Stress [MPa]	58	280
Fracture Energy [MN/m]	1.03×10^{-4}	1.05×10^{-5}
Plastic strain	-0.00147	-0.000296
Onset of crushing [MPa]	-8.61	-1.54
Critical compressive displ. [m]	-0.0005	-0.0005
Density [kton/m ³]	0.0023	0.0023

5.3.2 The steel material model

The steel is modeled by the SOLID Elastic material model in ATENA. In this model the steel material is simply elastic, with no maximum strength. The material description from GiD is shown in figure 5.7.

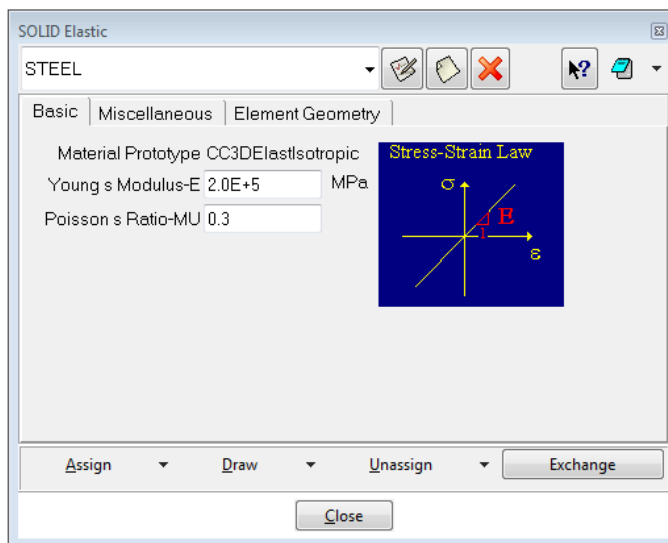


Figure 5.7: Material description for steel in ATENA

The purpose of the steel material is to act as a linear buffer between the applied forces and the highly nonlinear concrete material in order to avoid numerical instability in the models. The response of the steel frame is of no interest for the results. Hence this crude material representation is believed to be sufficient.

5.4 Loading and Boundary Conditions

In GiD the loading is imposed through accumulating intervals, which can be sub divided into load steps. To obtain a constant force through multiple intervals an applied load must be removed in the succeeding interval. It should be noted that this only applies to loads and not supports, as they have to be applied in each interval.

The models are loaded over four intervals. In the first interval the vertical pressure on the upper part has been applied as a line-load along with boundary conditions and monitoring points. These monitors are needed to generate the load-displacement curves. An example of this interval is shown in figure 5.8:

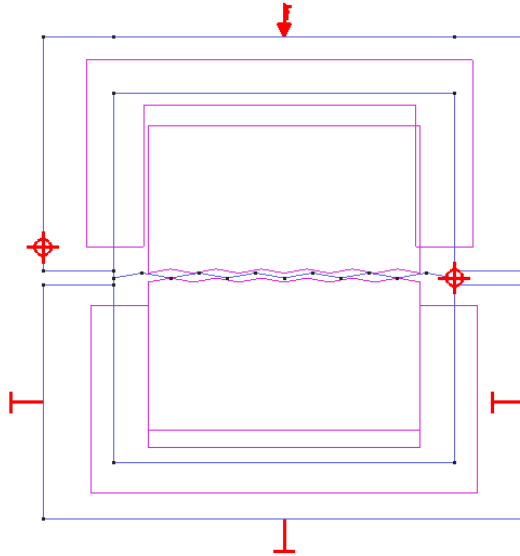


Figure 5.8: Loading and BC's of interval 1 for test 3.3.

NUMERICAL MODELS OF SLIDING STABILITY

The line-load for the different tests has been found by distributing the applied vertical force from Liahagen (2012) over the length of the samples (240mm). The applied line-loads are presented in the table below.

Table 5.2: Loading of the models.

Sample	From Liahagen				Modeled in ATENA			
	i [°]	δ_{Hmax} [mm]	N [kN]	ϕ_{max} [°]	i[°]	δ_H [mm]	Cohesion [kPa]	Q [kN/m]
1.1	40	15.23	27.52	73.08	0	20	1245	114.667
1.2	40	15.44	46.91	70.32	0	20	1720	195.458
1.4	40	26.34	68.49	69.52	0	20	2371	285.357
2.1	20	24.99	27.57	61.48	20	20	282	114.875
2.2	20	21.98	47.77	64.60	20	20	781	199.042
2.3	20	20.07	68.36	67.23	20	20	1552	284.833
3.1	10	33.16	24.82	54.95	10	20	309	103.417
3.2	10	32.94	45.98	51.93	10	20	382	191.583
3.3	10	33.23	67.65	51.63	10	20	536	281.877
4.2	0	33.23	67.23	37.74	0	20	62	280.125

In the second interval the pressure is removed and the horizontal force is applied trough prescribed deformation of ten millimeter at the left edge of the upper steel frame. Also in this interval master-slave boundary conditions are introduced along the upper edge. This interval is not active in the actual analyses. However, these master-slave boundary conditions are important to achieve plane horizontal displacement of the upper part. The loading of interval 2 is shown in figure 5.9 below.

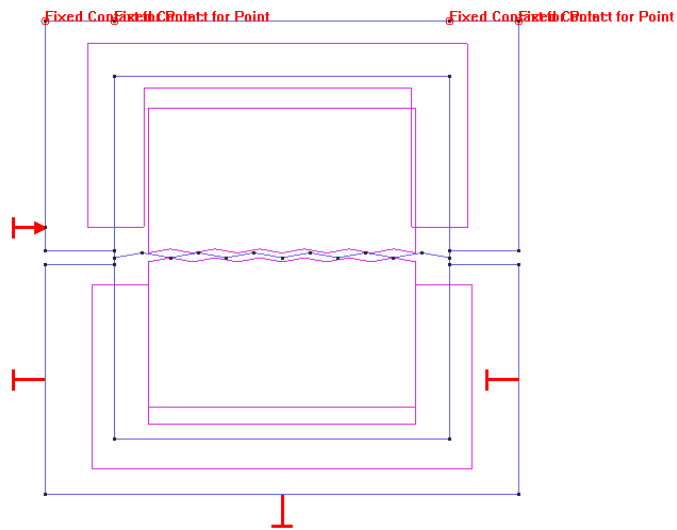


Figure 5.9: Loading and BC's of interval 2 for test 3.3.

Interval three and four are identical to interval two, except that the master-slave boundary conditions are removed.

5.5 Meshing

GiD offers two principally different strategies for meshing, structured or unstructured. However, the structured meshing algorithm is only applicable for models with simple, conventional geometry. In other words only test with a horizontal interface could be meshed with this algorithm. For consistency, the unstructured meshing algorithm has been used. The 2D models have been meshed with plane stress elements with a thickness (depth) of 240 mm.

When choosing elements both linear and quadratic variants of triangles/tetrahedral and rectangle/hexahedra have been tested. The linear triangle and rectangle elements are only able to present constant strain. Due to this simple representation of strains, these elements are known to produce overly stiff results, especially in bending (Cook et. Al 2002). In addition the linear elements may present spurious shear strain in plane strain problems which absorbs energy and also gives an overly stiff solution (Cook et. Al

2002). By refining the mesh, these problems may be overcome, but according to Cook et. Al (2002); convergence is slow.

It was quickly discovered that the linear elements gave too stiff results. For test 4.2 the initial 2D analyses with linear elements gave approximately 80% higher values for shear force compared to the analyses with quadratic elements. Compared to the actual results from Liahagen the quadratic elements gave the best match. For this reason the linear elements were abandoned and the rest of the analyses were run with quadratic elements.

As mentioned above the fineness of the mesh might improve the results of an analysis, especially when using linear elements. The goal for mesh fineness is to achieve the necessary accuracy by using only as many degrees of freedom (d.o.f) as necessary (Cook et. Al 2002). The simplest (and most unsophisticated) method to find out if the mesh is sufficient is to refine the mesh and run one more analysis with the new, finer mesh. If the results matches the ones obtained by the slightly courser mesh, this courser mesh is adequate.

By applying this simple test, it was found that an element size of approximately 1mm along the concrete – rock interface was sufficient. The mesh is shown in figure 5.10.

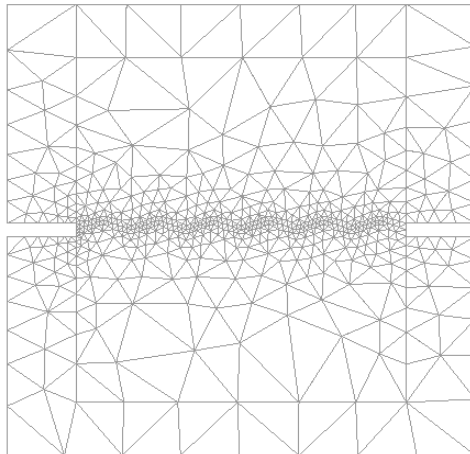


Figure 5.10: Mesh of test 2.2.

5.6 Analysis steps

Each of the intervals from GiD can be used to generate specific loads pr step in ATENA. This is done trough two parameters, the Interval Multiplier and Number of Load Steps. In figure 5.11 below the data for interval three of test 3.3 is shown.

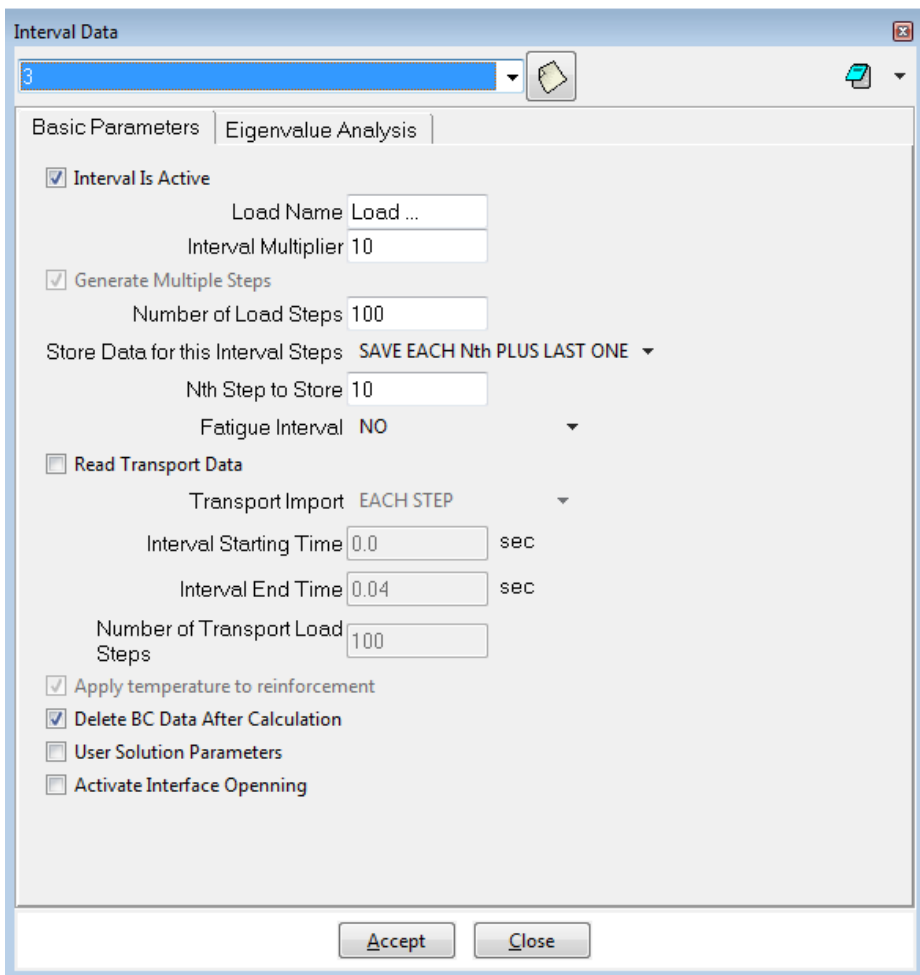


Figure 5.11: Interval Data.

The applied load in this interval is a prescribed displacement of 1 mm. The total displacement is therefore 10mm spread out over 100 load steps.

5.7 Ill-conditioning

Due to its uncomplicated geometry, test 4.2 from Liahagen (2012) was modeled first. However, getting results for this simple model proved harder than anticipated. The main problem was that the results (visualized by a load-displacement diagram) changed each time the model was analyzed. Many strategies were attempted to find the root of this instability, which heavily delayed the project. In the end a solution was found by reducing the interface stiffness K_{nn} and K_{tt} .

The instability in the analyses is an indication of an ill-conditioned system. This possibility was pointed out by Dobromil Pryl at Cervenka Consulting. Ill-conditioning is a term for situations where the computational accuracy (number of digits) is consumed when computing the stiffness matrix (Cook et. Al 2002). In other words; ill-conditioning is a result of very large and very small numbers in the same matrix. The common reason for ill-conditioning is a situation where stiff regions are supported by much more flexible regions. In the following it will be explained how use of the penalty method may lead to such situations.

Following Cook et. Al (2002); constraints in a system are imposed according to the following relation

$$\mathbf{C}\mathbf{d} - \mathbf{Q} = \mathbf{0} \quad (5.5)$$

Where \mathbf{d} is a vector containing the degrees of freedom (d.o.f). \mathbf{C} contains the d.o.f to be retained or “condensed out” and \mathbf{Q} contain eventual prescribed values of d.o.f. When using the penalty method the constraint relation (5.5) is written as

$$\mathbf{t} = \mathbf{C}\mathbf{d} - \mathbf{Q} \quad (5.6)$$

So that when $t = 0$ defines satisfaction of the constraints. The usual potential energy function Π_p can be expanded to include a so called *penalty function* $\mathbf{t}^T \alpha \mathbf{t} / 2$ where α is a diagonal matrix of penalty numbers. The expanded potential energy function can be written as

$$\Pi_p = \frac{1}{2} \mathbf{d}^T \mathbf{K} \mathbf{d} - \mathbf{d}^T \mathbf{r} + \frac{1}{2} \mathbf{t}^T \alpha \mathbf{t} \quad (5.7)$$

The penalty of violating constrains increases with increasing α . From the above equations and the minimum condition $\{\partial\Pi_p / \partial\mathbf{d}\} = \{0\}$ the following is obtained

$$(\mathbf{K} + \mathbf{C}^T \alpha \mathbf{C}) \mathbf{d} = \mathbf{r} + \mathbf{C}^T \alpha \mathbf{Q} \quad (5.8)$$

In which $\mathbf{C}^T \alpha \mathbf{C}$ can be called a *penalty matrix*. If α is zero the constraints are ignored, and as α grows d changes so that the constraints are more nearly satisfied. However, a large α -matrix may lead to situations where the stiffness in the contact elements becomes vastly greater than the stiffness in the surrounding elements. This can again lead to numerical problems due to ill-conditioning.

In ATENA the penalty numbers are given by the analyst in form of initial stiffness of the interface material. As described in section 5.4 it is advised that this stiffness is approximately ten times the stiffness of neighboring elements. The resulting interface stiffness according to this estimate, with $E_{rock} = 100\,000$ MPa and element sizes of approximately 1mm close to the interface then becomes 1×10^9 .

This resulted in numerically unstable results, and reducing the values for interface material stiffness has been the most influential parameter for achieving stable results. However, in order to satisfy the contact constraints large penalty numbers are required. Therefore many analyses were conducted to find the highest possible interface material stiffness which presented reliable, stable results.

The process of finding this interface stiffness had to be conducted manually. Naturally this procedure was very time-consuming, but considering the improvement of the results, it was necessary. In general values of K_m in the area of 10^4 and K_t around 10^3 have proven to provide a good balance between analysis stability and proper results. The fine tuning of these parameters was enabled trough comparison with the results from the tests. The updated stiffness-values are presented in the table below:

Table 5.3: Interface stiffness values

Sample	K_{nn} [MN/m ³]	K_{tt} [MN/m ³]	K_{nn}^{min} [MN/m ³]	K_{tt}^{min} [MN/m ³]
1.1	1.00×10^4	6.00×10^2	1.00×10^2	6.00
1.2	1.00×10^4	2.00×10^3	1.00×10^2	2.00×10^1
1.4	1.00×10^4	2.00×10^3	1.00×10^2	2.00×10^1
2.1	1.00×10^4	1.00×10^3	1.00×10^2	1.00×10^1
2.2	1.00×10^4	2.00×10^3	1.00×10^2	2.00×10^1
2.3	1.00×10^4	3.00×10^3	1.00×10^2	3.00×10^1
3.1	1.00×10^4	2.00×10^3	1.00×10^2	2.00×10^1
3.2	1.00×10^4	2.00×10^3	1.00×10^2	2.00×10^1
3.3	1.00×10^4	2.00×10^3	1.00×10^2	2.00×10^1
4.2	1.00×10^4	6.00×10^3	1.00×10^2	6.00×10^1

The effect of too soft interface stiffness is illustrated in figure 5.12 below.

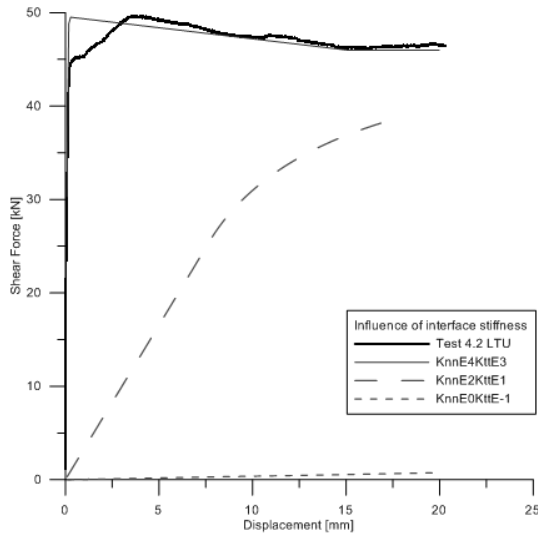


Figure 5.12: Influence of interface material stiffness for test 4.2.

5.8 Modeling a full scale dam

For a full scale dam, the modeling of each asperity is overly labor-intensive. Thus a simplified approach may be applied. To avoid modeling the exact interface, the formulation presented by Patton (1966) where the asperity angle is included in the frictional parameter is applied. In chapter four it is seen that this formulation alone does not describe the peak shear capacity sufficiently. To improve this, the cohesive parameter representing the cut-off of micro roughness is included. This leads to the following hybrid formulation for shear capacity

$$\tau = c + \sigma_n \cdot \tan(\phi_{residual} + i) \tag{5.9}$$

To check the validity of this formulation, equation 5.9 has been applied to test series two, three and four from Liahagen. The results of these calculations are showed in the table below.

Table 5.4: Shear capacity from equation 5.9.

test	i [°]	N [kN]	V [kN]	Φ_b [°]	Cohesion [kPa]	$A_{coh.}$ [m ²]	V_{calc} [kN]	Error [%]
2.1	20	27.57	50.74	34.38	287	0.030658	47.13	7
2.2	20	47.77	100.59	“	781	“	90.62	10
2.3	20	68.36	162.83	“	1552	“	142.99	12
3.1	10	24.82	35.38	“	309	0.029238	33.32	6
3.2	10	45.98	58.70	“	382	“	56.16	4
3.3	10	67.65	85.43	“	536	“	81.87	4
4.2	0	67.23	49.56	“	62	0.0576	49.57	0.02

The results in table 5.4 show that equation 5.9 represents the shear capacity reasonably well. The errors are calculated according to equation 4.3 and show increasing errors for increasing asperity inclination. All the calculated shear forces are lower than the ones obtained in the actual tests. However, due to the great variance in the cohesive parameter it is decided to only use the value from test 4.2 which is 62 kPa in the further analyses. This is the lowest observed value for the cohesion, and is in that way a conservative estimate.

To illustrate this approach a section of dam Ipto has been modeled. This dam is a concrete gravity dam located in Nordland County in northern Norway, and does not meet the stability requirements for neither sliding nor

overturning. For the modeling a 5.5 meters high section is chosen. The geometry and loading are found from the reconsidering report (Sweco 2007), and a sketch of the geometry is shown in figure 5.13 below. In the numerical models the protective wall at the dam crown has been excluded.

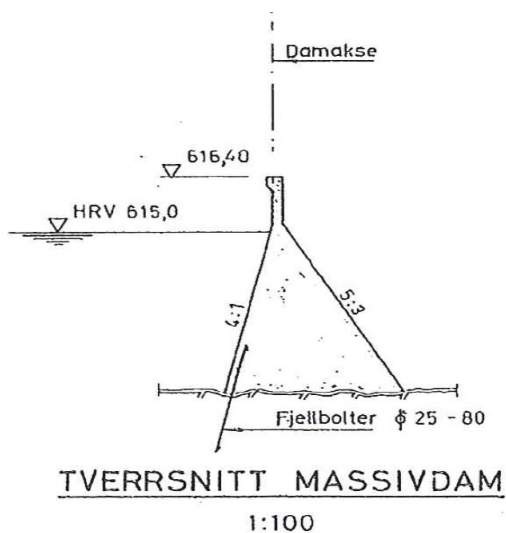


Figure 5.13: Dam Ipto (Sweco 2007)

It must be emphasized that the scope for the following analyses is to illustrate how the roughness will influence the calculated stability of a dam. The results obtained are therefore not to be seen as correct assessments of the stability towards sliding for the Ipto dam.

The model uses the same rock and concrete material models as used in the models of Liahagen's shear tests. However, the material parameters for the concrete are changed to represent a C20/25 which is believed to be more in line with the actual dam. The material parameters for the concrete are listed in the table below:

NUMERICAL MODELS OF SLIDING STABILITY

Table 5.5: Material parameters for C 20/25 concrete in ATENA

Material parameters	
Young's Modulus [GPa]	30
Poisson's Ratio	0.2
Tensile strength [MPa]	2.2
Compressive Failure Stress [MPa]	28
Fracture Energy [MN/m]	5.5×10^{-5}
Plastic strain	-0.000933
Onset of crushing [MPa]	-4.62
Critical compressive displ. [m]	-0.0005
Density [kton/m ³]	0.0023

As seen in figure 5.14 below the ice is modeled as a separate material. This is done for the same reason as the steel frame was added to the models of Liahagen's tests, and the ice is modeled with the same steel material model as used in those models.

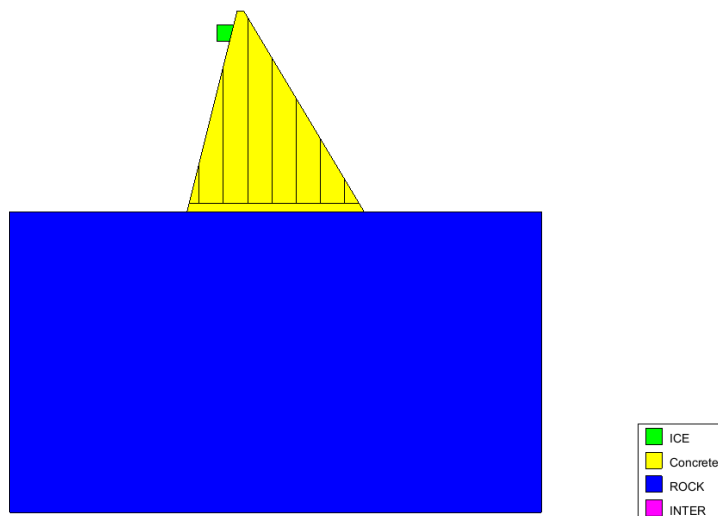


Figure 5.14: Model of Dam Ipto.

The section has been modeled with two different frictional parameters for the interface, representing zero and ten degrees asperity inclination. To assess the effect of micro roughness the models have been analyzed with a cohesive

parameter of both 62 and 1 kPa. For convenience the analyses have been labeled A, B and C, and the interface parameters for each test are presented in table 5.6 below.

Table 5.6: Interface parameters

Analysis Name	Φ_b [°]	i [°]	Cohesion [kPa]	Tensile Strength [kPa]
A	34.38	0	1	0.5
B	34.38	10	1	0.5
C	34.38	10	62	31

For these models the normal and tangential stiffness of the interface (K_{nn} and K_{tt}) was initially set according to the Troubleshooting manual (Pryl 1013). As for the models of Liahagen’s tests this gave unstable analyses. For this dam, there are no tests to calibrate against. In other words the exact capacity is not known. Thus, a parametric study on the influence of K_{nn} and K_{tt} had to be conducted. The parametric study is presented in APPENDIX F, and for the further analysis parameters giving the lowest shear capacity from this study is used. Hence, the analyses are run with values of $2.5 \cdot 10^5$ and $1.04 \cdot 10^5$ [MN/m³] for K_{nn} and K_{tt} respectively, and a mesh size of 400mm. To better illustrate the difference in shear capacity from including the cohesion, no cohesion softening has been used in these analyses.

The section is loaded in successive load intervals each containing 50 or 100 load steps to resemble the actual load history of a dam. The principle of the loading is to apply the loads as they would appear for a newly constructed dam and is showed in table 5.6 below. To get the failing history of the dam extra loads in form of increasing ice forces are applied. However, due to the brittle characteristics of the interface material failure the analyses crash when the shear capacity was reached. To overcome this problem a conditional break criterion is applied (see APPENDIX G) along with very small loads per step from this point. As a result, the amount of “extra” ice forces has to be adjusted for each analysis individually.

NUMERICAL MODELS OF SLIDING STABILITY

Table 5.7: Applied loads of the dam section.

Load Interval / Load Steps	Load description	Horizontal load [kN]	Vertical load [kN]
1 / 1 – 50	Own weight of dam	-	367
2 / 51 - 150	Hydrostatic pressure	150	38
3 / 151- 250	Uplift	-	- 137
4 / 251 – 350	Ice	100	-
Total number of load steps varies for each analysis	Increased Ice	varies	-

The results are obtained from monitors of reactions at the supports and monitors of displacement at the dam. The loading, monitors and constraints of load interval one are shown in figure 5.15 below.

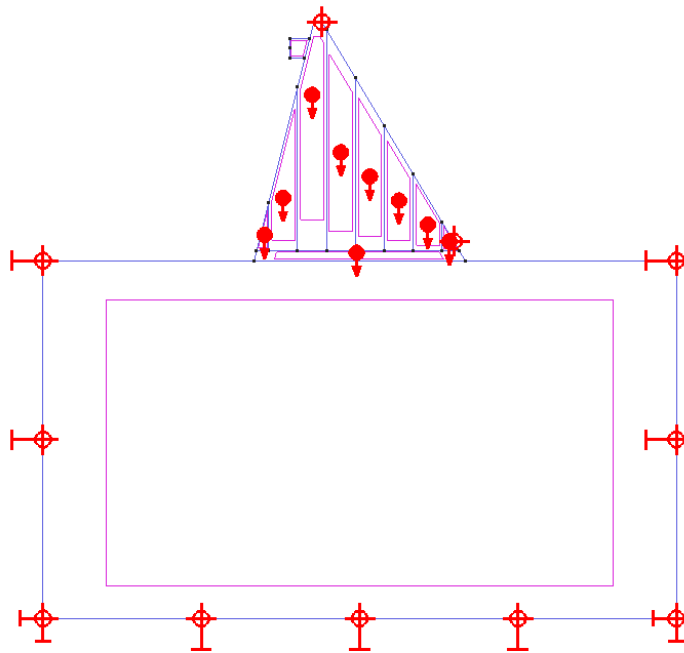


Figure 5.15: Imposed conditions in load interval one.

6. RESULTS AND DISCUSSION

In this chapter the results from the finite element analyses are both presented and discussed. The reason for combining the discussion and the presentation of results in one chapter is to reduce the risk of misunderstandings and confusion by processing the results of the shear test analyses completely before presenting the results from the analyses of dam Ipto.

The chapter is subdivided in three sections. In the first section the results from the analyses of Liahagen's tests are presented along with brief comments. In section 6.2 the results are thoroughly discussed in order to assess the quality and usability of the numerical models. In the last section the results from the full scale dam is presented.

6.1 Comparison of Liahagen's tests

Co-supervisor Gabriel Sas provided the excel files with results from Liahagen's shear tests. The results from the numerical analyses have been computed by monitoring the horizontal displacement and reaction-force along the loaded edge of the model. The load-displacement curves from the analyses are presented in the same diagrams as the curves from the actual tests. For the sake of report consistency the results are presented in the same order as done in chapter four.

6.1.1 Test 4.2

The results from the analyses of test 4.2 are compared to the exact values in the load-displacement diagram shown in figure 6.1 below.

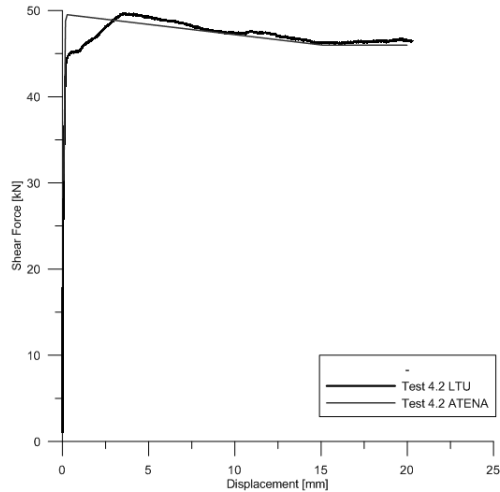


Figure 6.1: Test 4.2

From figure 6.1, it is seen that both the peak and residual shear capacity is well described by the approach and parameters found in chapter four. However, the actual peak shear capacity⁷ is reached for a somewhat larger displacement compared to the numerical values. The reason for this discrepancy is that cohesion stiffening is not included in the numerical model as described in section 5.2.

6.1.2 Test series 3

The load-displacement curves from test series three are shown in figure 6.2 to 6.4 below. In line with the discussion in chapter four it is chosen to stop the displacement at 20 mm, when the concrete sample slides over the asperities. These tests show pure sliding failure with no shearing of the concrete or rock material.

⁷ When disregarding the “peak” at 33 mm of displacement as done in chapter four.

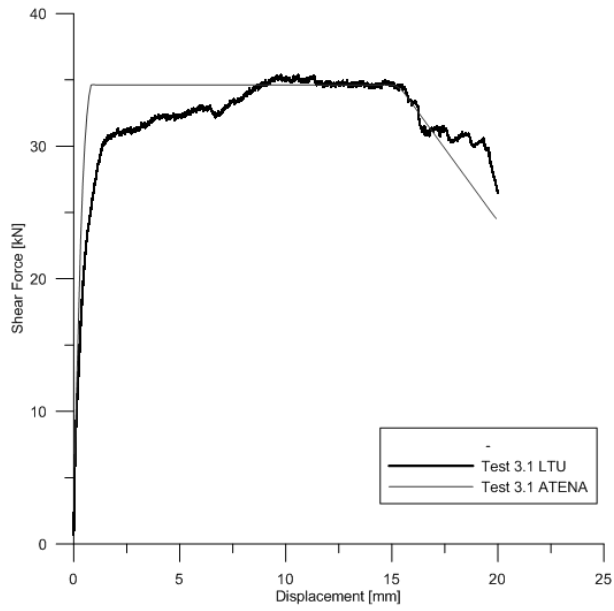


Figure 6.2: Test 3.1

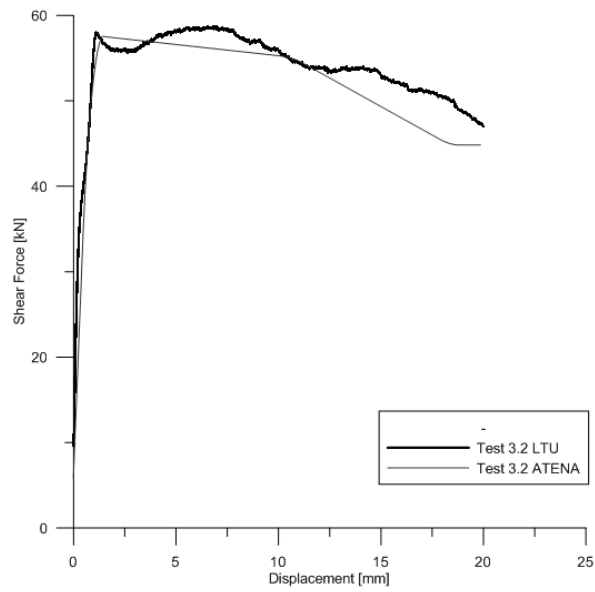


Figure 6.3: Test 3.2

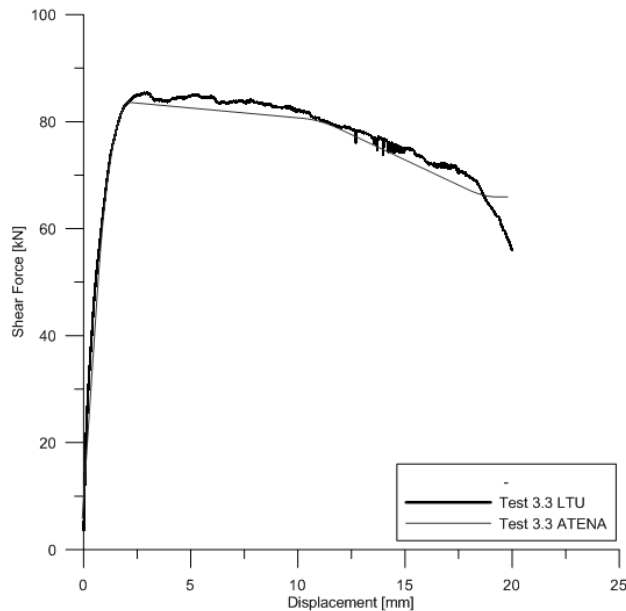


Figure 6.4: Test 3.3

The figures above show that the parameters found from chapter four provide a good match for the peak shear capacity. The residual capacity is not so well described. A possible reason for this is that the increase in normal force from the actual tests not is included in the analyses. Alternatively the interface for test 3.1 and 3.3 are more heavily degraded for these tests compared to test 4.2, which in return results in a somewhat lower residual friction angle for these tests. In the same way test 3.2 might experience less degradation of the interface compared to test 4.2. Test 3.1 shows some of the stiffening behavior as test 4.2 and requires even more displacement to reach full capacity.

6.1.3 Test series 2

The tests in series two experience both a sliding and shearing failure. However for the numerical analyses only sliding failure is obtained. The reason for this is believed to be related to the material parameters and will be discussed further for test series one below. The results are presented I figure 6.5 to 6.7 below.

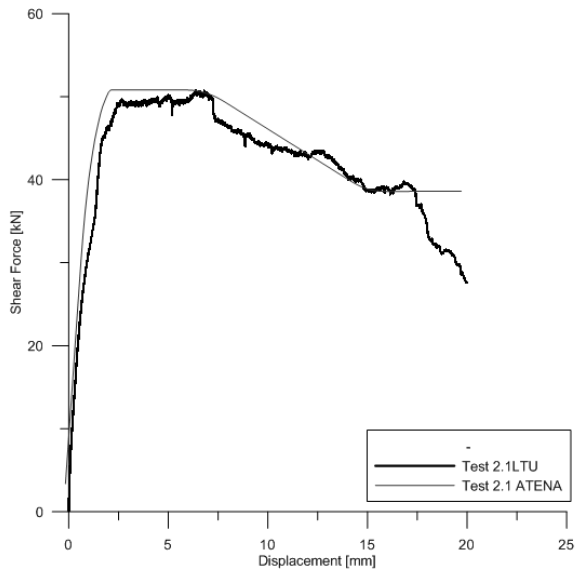


Figure 6.5: Test 2.1

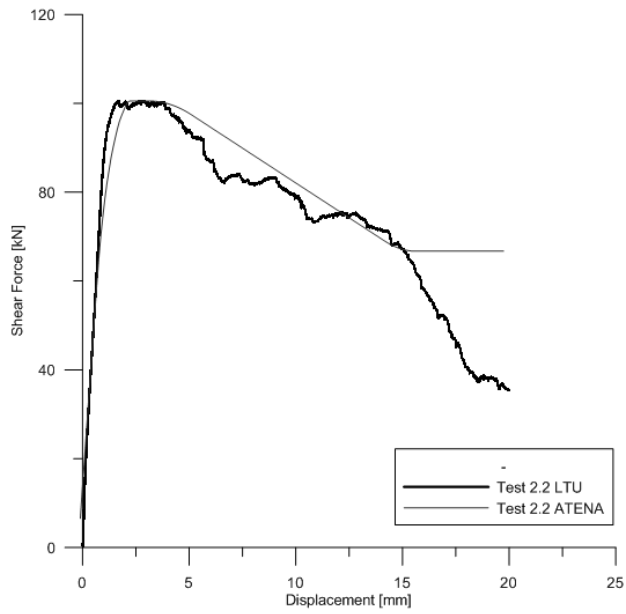


Figure 6.6: Test 2.2

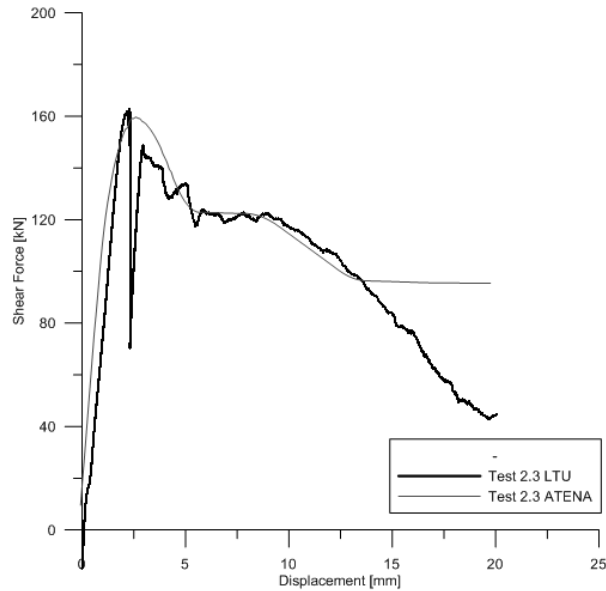


Figure 6.7: Test 2.3

For this test series the residual capacity is well represented for a displacement of about 15 mm, but does not describe the further decline of capacity following this point. The reason for this is believed to be that the models do not express the shearing failure explained in chapter four, which leads to a larger residual asperity inclination and a higher residual capacity. The peak shear capacity is well described, and the expected errors mentioned in section 4.3 are not seen. The reason for this is also believed to be that the shearing of material is not represented.

6.1.4 Test series 1

The tests in series one all experienced a shearing failure of the concrete asperities, and not sliding along the interface. This failure mode has been hard to obtain from the numerical models. The main reason for this is that the analyses crash after the material starts to crack due to instability problems with zero or negative Jacobian for the stiffness matrix. This error message is an indication of an ill-conditioned system (Pryl 2013)

As described in chapter five, the strategy for obtaining material failure has been to apply an interface with high cohesive values, and gradually reduce the tensile strength and the onset of cracking for the concrete material. In figure 6.8 the concrete material failure is shown. The blue field in the left part indicates that the tensile strength of the material is reached. The black dots in this area represent cracks in the concrete.

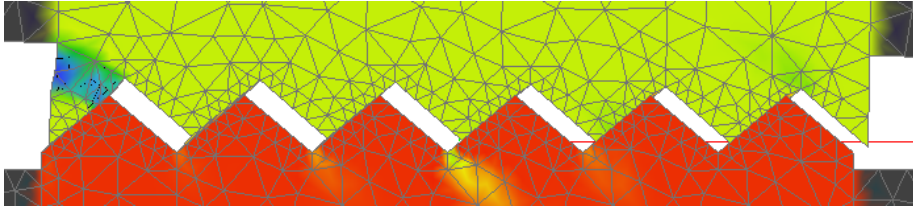


Figure 6.8: Cracking of concrete material for test 1.1

One attempt was also made to model test 1.4 without interface material. The failure of this model is shown in figure 6.9

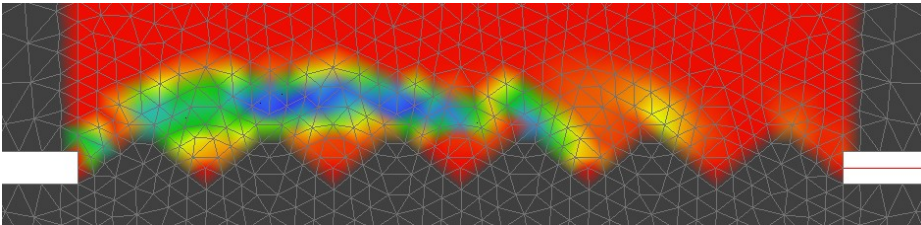


Figure 6.9: Material failure for test 1.4.

Due to the numerical instability problems only the peak shear capacity was obtained from these analyses. However, this capacity is governed by the concrete material parameters alone, and not by the interface parameters. From Liahagen, only the compressive strength was given for the rock and concrete materials, thus the tensile strength and onset of crushing have been found from the default values.

For a concrete with compressive strength of 58 MPa, the default value of tensile strength is 4.1 MPa in ATENA. However, to obtain the peak shear capacity described by Liahagen, the tensile strength needed to be reduced to 1.5 MPa. Since the actual value for tensile strength not given, the validity of these results are hard to assess.

RESULTS AND DISCUSSION

The results from the analyses with flat interface are presented in figure 6.10 to 6.12. The load displacement curves are marked with a * to indicate that these results are obtained trough analyses with simplified interface geometry.

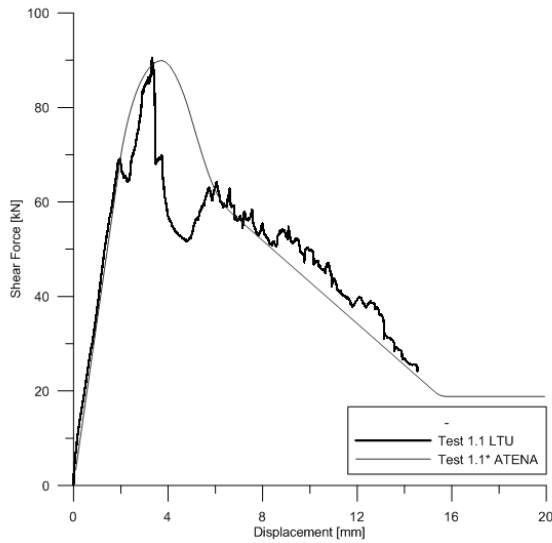


Figure 6.10: Test 1.1

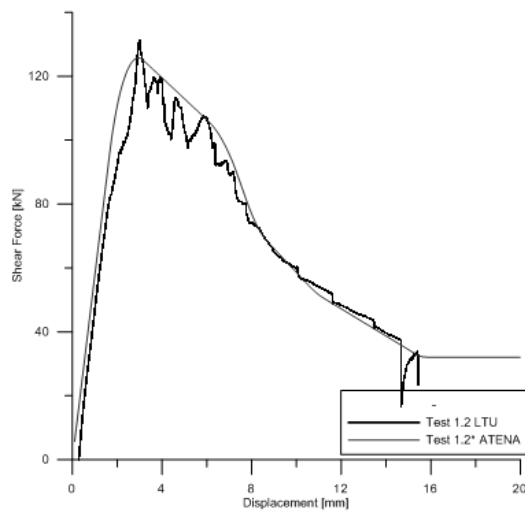


Figure 6.11: Test 1.2

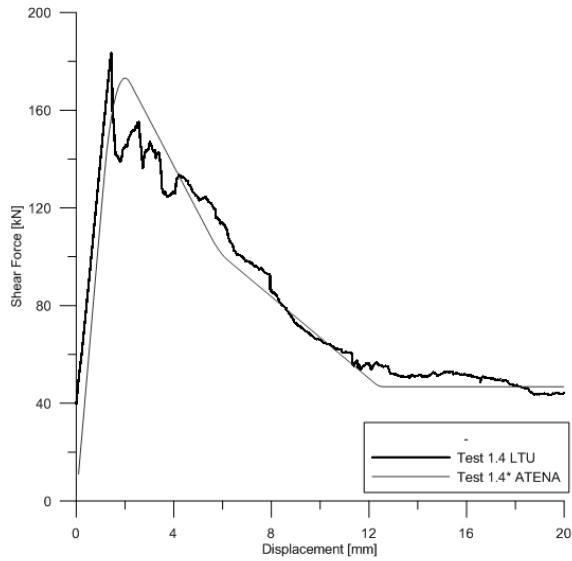


Figure 6.12: Test 1.4

These results show good representation of both the peak and residual shear capacity, even though the failure mode is not described correctly. This indicates that a simplified approach to the geometry might give sufficient results as long as the cohesive parameter can be calibrated by physical tests.

From section 4.4 it was suspected that this method would give large errors due to the representation of the residual sliding plane by the residual friction angle found from test 4.2. It appears that these suspicions were groundless as the residual capacity is sufficiently described in the numerical models.

6.1.5 Tests with bond

Due to the difficulties regarding representation of material failure results from test 1.3H has not been achieved. In figure 6.13 the results from the analysis of test4.1H is shown.

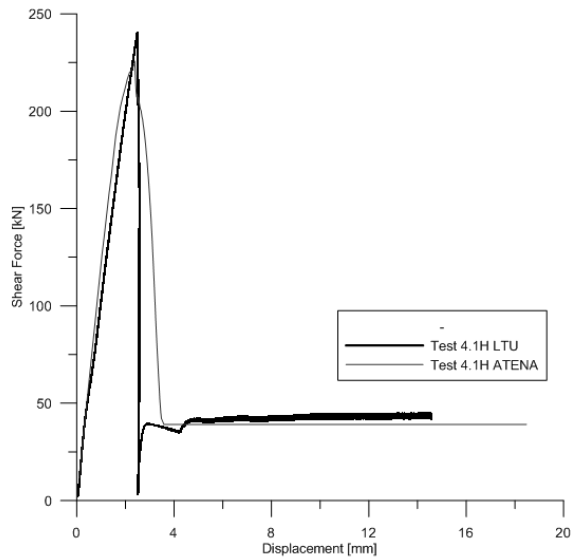


Figure 6.13: Test 4.1H

The peak value is not reached for this analysis, but the representation of the residual shear capacity is good. The failure of the actual test is completely brittle, and a large part of the capacity is lost in one instant. For the numerical models this introduces complications in the iterations at this point. In order to avoid numerical problems a small ductility is applied through cohesion softening.

6.2 Discussion of the numerical results

In general it is seen that the procedure and values found in chapter four gives a good representation of both the peak and residual shear capacity. Coupled with a softening behavior of the cohesive parameter the shear capacity for the failure history of the actual tests has been represented sufficiently. Sufficient representation of the concrete asperity cut-off observed in test series one and two has not been achieved.

The procedure from chapter four should give results that match both the peak and residual shear capacity from the tests exact. However, studying the numerical results, it is clear that some errors still occur. The difference between the peak shear capacity from the laboratory tests and the numerical analyses are listed in table 6.1.

Table 6.1: Error in peak shear capacity from the numerical models.

From Liahagen		Modeled in ATENA		
Sample	V_{\max} [kN]	V_{peak} [kN]	Error	
			[kN]	[%]
1.1	90.53	89.91	0.62	0.68
1.2	131.19	125.80	5.39	4.11
1.4	183.42	173.21	10.41	5.68
2.1	50.74	50.81	0.07	0.14
2.2	100.59	100.57	0.02	0.02
2.3	162.83	162.08	0.75	0.46
3.1	35.38	34.65	0.73	2.06
3.2	58.70	57.56	1.14	1.94
3.3	85.43	83.65	1.78	2.08
4.1H	240.00	225.75	14.25	5.94
4.2	49.56	49.52	0.04	0.08

The error-% is calculated with respect to the actual value from Liahagen, according to equation 4.3. On average the error is around 2% with a maximum of 6% for two analyses. Compared to the results from the Mohr-Coulomb and Patton criteria in chapter 4 this is a great improvement.

The reason for these errors is hard to pin-point. One possible source is inaccurate readings of the residual capacity in Liahagens tests. This value

RESULTS AND DISCUSSION

influences the cohesive value calculated in chapter four and can in such a way affect both the representation of peak and residual shear capacity. Due to the fact that stable analysis with cracking of concrete was not obtained, the residual capacity is only describing the capacity as long as the interface asperities are intact. This explains why the residual capacity is not well represented for test series two. For test series one this problem is avoided as the interface is modeled with the inclination of the residual sliding plane from the actual tests.

Another source of error might be the values of K_{nn} and K_{tt} . As described in section 5.2 these parameters both govern the physical behavior of the interface, but also acts as penalty numbers for the contact constraints. These parameters were determined based on a balance between stability of the analyses and proper results. The course parametric study of the influence of these parameters presented in section 5.7 indicates that setting these parameters too low will reduce the shear capacity of the numerical models. Hence, further fine tuning of these parameters might give a somewhat more accurate representation of the shear capacity.

It is hard to determine why the material failure in the concrete not was obtained. Proper input values for the tensile strength and onset of crushing would improve the material models and ease the refinement of these. With so many parameters lacking, a full parametrical study would be needed to fine-tune the materials. For this Thesis the time-frame did not allow such extensive testing.

The results from the analyses show that the actual shear capacity of the tests are better represented through numerical modeling than the formulations available for hand calculations. Especially the possibility to represent the softening behavior after peak shear capacity is reached is a large benefit.

The costs for achieving such improved results are that the interface geometry must be modeled exact and that physical tests are needed to calibrate the models.

6.3 Results from full scale dam analyses

The results of the analyses of dam Ipto are presented in figure 6.14 below.

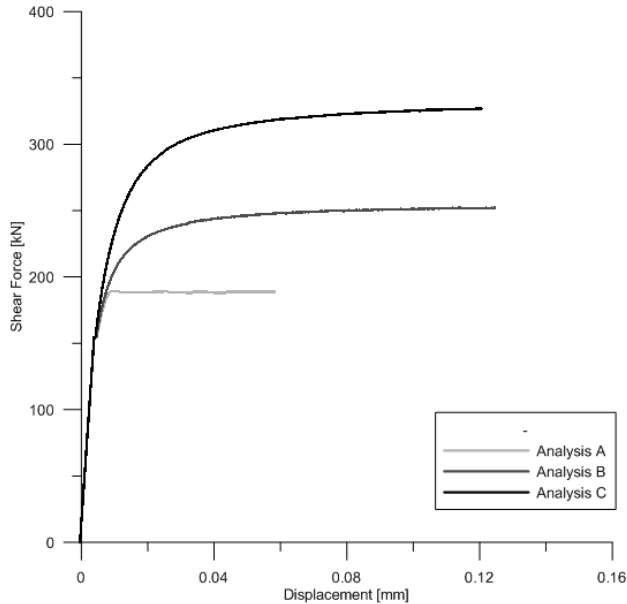


Figure 6.14: Results from analyses of dam Ipto.

As seen in figure 6.14, the effect of macro and micro roughness is an increased shear capacity. In table 6.2 the factor of safety is calculated by dividing the shear capacity found from the analyses on the horizontal design load (water pressure and ice force), similar to what is done in the shear friction method used today.

Table 6.2: Factor of safety from finite element analyses.

Analysis Name	N	V_{capacity}	V_{design}	Factor of safety
A	268	188	250	0.75
B	268	252	250	1.01
C	268	326	250	1.30

It must be emphasized that these analyses only serve as an example, as the input parameters for the interface is taken from Liahagen's tests, and therefore cannot be expected to represent the actual conditions at the dam site.

RESULTS AND DISCUSSION

The shear capacity is stress related and one of the arguments of assessing the stability of sliding by finite element analyses is that the hand calculations only consider the average stresses under the dam section. As mentioned in section 5.8 the Ipto dam is considered unstable towards both sliding and overturning. Thus the interface stresses are analyzed to give a more realistic assessment of the dam's total stability.

Studying the displacements and stresses at the interface, analysis A show a regular sliding failure, while analysis B and C show a combination of overturning and sliding. The reason for this is that with an increased shear capacity, larger ice forces are needed to get failure. Due to the location of the ice, increasing this load will affect the stability towards overturning as well as sliding.

This combined failure mode cause high tensile stresses at the interface. The tensile stresses first appear at the upstream end of the interface at around load step 150 and propagate towards the downstream end as the loading increases. In figure 6.15 the shear stresses at the interface for the last load step of analysis C is shown (note that the displacements are magnified with a factor of 100).

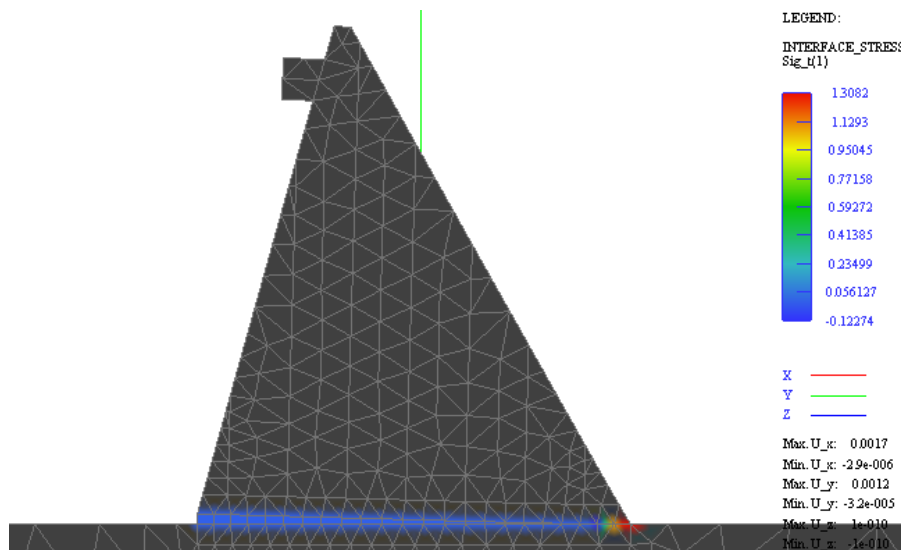


Figure 6.15: Interface shear stresses for analysis C (numbers in MPa).

As shown in figure 6.15 above, only a small part at the downstream end of the dam transfers shear stresses, which means that only this small part have compressive stresses. This redistribution of stresses might explain the somewhat more ductile behavior of analysis B and C compared to analysis A.

The fact that the shear capacity is reached in combination with an overturning failure are in line with the theory presented by Fishman (2007, 2008 and 2009) and indicates that the sliding and overturning stability of a concrete dam is linked, at least for gravity dams. A thorough assessment of the Ipto dam's stability towards overturning falls outside the scope for this Thesis, but investigating the combined failure of overturning and sliding could form an interesting foundation for further work.

If equation 5.9 was transferred to force-form and included as the shear capacity in the shear friction method (equation 3.1) the factors of safety would have been higher compared to the numerical results for analyses B and C. Especially the effect of micro roughness seems to give a smaller contribution in the analyses.

The source for this reduction is that tensile normal stresses are inputted in equation 5.9 with a negative sign. For contact elements with tensile stresses the shear capacity is reduced until the stresses reach the tensile strength of the element (illustrated in figure 5.4.), in other words, the effect of cohesion is greatly reduced as most of the elements along the interface show tensile stresses. This effect is not accounted for in the hand calculations as the net normal force is positive (compressive).

Even though these analyses show that the effect of micro roughness through the cohesion parameter is reduced, it still has an influence on the peak shear capacity. In Liahagens tests the contribution from micro-roughness exhibit great variance, which indicates that for a full scale dam extensive sampling and testing might be required to obtain a proper input value for the cohesion parameter. It should also be noted that from the literature study in the author's project work it was found that the shear capacity of an interface might be scale dependent.

RESULTS AND DISCUSSION

The amount of input parameters needed combined with possible scale effects, leads the Author to believe that large scale physical tests of dam sliding might be necessary to utilize the full potential of the finite element analyses.

As seen in section 5.8, the governing equation for shear capacity used in this model (equation 5.9) show around ten percent error for the peak shear strength when compared to the tests from Liahagen. Compared to the errors listed in table 6.1 this method is clearly not as accurate as the analyses of the tests, but still better than the available methods for hand calculations.

7. CONCLUSIONS

The analyses of the shear tests conducted by Simen Liahagen show that to describe the shear capacity of a sliding plane, more sophisticated formulations are needed compared to the ones used today.

The shear capacity of a sliding plane is governed by two failure mechanisms. For a bonded interface, sliding is a result of a material failure at one or both of the adjoining materials. For an un-bonded interface, the capacity might be governed by both a sliding failure over the roughness and a material failure in parts of the roughness. From the analyses of Liahagen's shear tests it is found that which failure mode that govern the capacity is dependent on both the normal stress and the inclination of the interface roughness.

The shear tests indicate that if the surface roughness is not cut-off, it contributes to the shear capacity in two ways. Firstly, the macro-roughness, or asperities, along the sliding plane increase the shear capacity by tilting the plane of the actual shear failure. Secondly, the micro roughness along these asperities is cut off for a sliding failure. This contribution to the total shear capacity is greater than tilting the sliding plane.

By analyzing the tests with the finite element method not only the peak shear capacity is described, but also the softening behavior of micro-roughness cut-off. This provides models where the failure history is obtained, and in such a way enables more realistic analyses of actual sliding failure.

The simplified approach to assessing the stability towards sliding of dam Ipto through finite element analyses show that the contribution from surface roughness might be somewhat smaller compared to the tests due to tensile stresses at the interface. However, to verify the accuracy of this method the interface parameters must be found from the actual dam site. For this purpose large scale shear tests will provide important results for calibration of the numerical interface material model, and in addition indicate how scale effects influence the shear capacity.

CONCLUSIONS

To further develop the method for full scale dam assessment, investigating the effect of other interface conditions than the roughness is needed. Hence, the following subjects might form the basis for further work on the topic:

- Investigating the influence of scale effects on the shear capacity to secure reliable input parameters for the sliding behavior.
- Investigating how rock bolts and varying roughness along the sliding plane affects the shear capacity and in turn the stability towards sliding.
- Investigating how the shear capacity can be found for a partly bonded sliding plane.
- Investigating how the total stability of the dam evolves through a combined sliding-overturning failure.

From the analyses in this Thesis, two main advantages with finite element analyses of stability towards sliding of dams are seen. Firstly, this method can address the shear capacity on stress-form instead of force-form. Secondly the finite element method is able to describe the actual failure mechanisms governing the shear capacity. This provides a huge improvement in achieving realistic assessments of the stability compared to today's methods using equilibrium of averaged forces.

Such improved methods will secure that unnecessary funds not are used on dam rehabilitations. In the long run this will provide more sustainable dams and a more rational distribution of resources.

REFERENCES

- Bandis, S.C.; Lumsden, A.C.; Barton, N.R., (1981). Experimental studies of scale effects on the shear behavior of rock joints, *Int. J. Rock Mech. and Min. Sci.*, Vol. 18, No. 1, pp. 1-21.
- Barton, N., (1973) Review of a new shear-strength criterion for rock joints. *Engineering Geology* vol 7, pp: 287-332.
- Barton, N., Bandis, S., (1982). Effects of block size on the shear behavior of jointed rock. 23rd U.S. Symp. On Rock Mechanics pp: 739-760.
- Barton, N., Choubey, V., (1977). The Shear Strength of Rock Joints in Theory and Practice. *Rock Mechanics* vol 10, pp: 1-54
- Cervenka, V., Jendele, L., Cervenka, J., (2012) ATENA Program Documentation, Part 1: Theory. http://www.cervenka.cz/assets/files/atena-pdf/ATENA_Theory.pdf
- Cervenka, V. Cervenka, J. Zednek, J. Pyl, D. (2013) ATENA program Documentation, Part 8: User's Manual for ATENA_GiD Interface. http://www.cervenka.cz/assets/files/atena-pdf/ATENA-Science-GiD_Users_Manual.pdf
- Cook, R., D., Malkus, D., S., Plesha, M., E., Witt, R., J., (2002) Concepts and applications of finite element analysis. Fourth Edition. University of Wisconsin – Madison. USA
- Eltervaag (2012) Sliding Stability of Lightweight Concrete Dams, Contribution from Surface Roughness. Project. NTNU, IKT Trondheim, unpublished.
- Energi Norge (2012). Optimal og sikker rehabilitering av betongdammer: Glidestabilitet av betongdammer. Preliminary unpublished, conducted by Norconsult.
- Fishman, Y. A. (2007). Features of shear failure of brittle materials and concrete structures on rock foundations. *International Journal of Rock Mechanics and Mining Science* 45, p: 976–992.
- Fishman, Y. A. (2008). Features of compressive failure of brittle materials. *International Journal of Rock Mechanics and Mining Science* 45, p: 993–998.
- Fishman, Y. A. (2009). Stability of concrete retaining structures and their interface with rock foundations. *International Journal of Rock Mechanics and Mining Science* 46, p: 957–966.
- Johansson, F., (2009). Shear Strength of Unfilled and Rough Rock Joints in Sliding Stability Analyses of Concrete Dams. Ph.D. Thesis. Royal Institute of Technology (KTH), Stockholm.

Johansson, F., Gustafsson, A., Rytters, K., Stille, H., (2012). Proposal for new Swedish guidelines with respect to sliding stability of concrete dams founded on rock. Workshop: Bærekraftig forvaltning av Betongdammer, Narvik 23.-24. October 2012. Norut. Conducted by KTH and Sweco.

Jørstad, O., A., (2009). Skjærstyrke mellom pilarer og fundament for lette betongdammer. ProjectNTNU, IVT Trondheim, unpublished

Liahagen, S., (2012) Stabilitet av betongdammer - Ruhetens påvirkning på skjærkapasiteten mellom betong og berg. Master's Thesis. NTNU,IVM, Trondheim, unpublished.

Nicholson, G.A., (1983). Design of gravity dams on rock foundations: sliding stability assessment by limit equilibrium and selection of shear strength parameters. Geotechnical Laboratory, U.S. Army Corps of Engineers, Waterways Experiment Station.

Nilsen, B., Thidemann, A., (1993) Rock Engineering, Norwegian Institute of Technology, Division of Hydraulic Engineering, Trondheim.

NVE, Norwegian Water Resources and Energy Directorate, (2005), Retningslinje for betongdammer.

Patton, F.D (1966). Multiple modes of shear failure in rock. 1st ISRM Congress, September 25 – October 1, 1966, Lisbon, Portugal. LNEC

Pryl, D., Cervenka, V. (2013) ATENA Program Documentation, Part 11: Troubleshooting manual. <http://www.cervenka.cz/assets/files/atena-pdf/ATENA-Troubleshooting.pdf>

Sas,G., Daescu, C., Sæther, I., Arntsen, B. Målset Dam – Finite element analysis assisted by tests. Technical report, preliminary not published

Stølen, P., (2012) Målsetdammen – sikkerhet mot glidning i platedam. Master's Thesis. NTNU, IVM, Trondheim, unpublished.

Sweco, (2007) Skjomen – Revurdering av Ipto- og Kjårdadammen, technical report.

United States Department of the Interior Bureau of Reclamation, USBR (1977). Design Criteria for Concrete Arch and Gravity Dams. Engineering Monograph No. 19. U.S.Government Printing Office.

DIGITAL APPENDIX

The following files are appended digitally in the delivery system for Master's Theses' (DAIM) at NTNU

Text and excel files:

PROJECT.pdf

IPTO.xlsx

IPTO3.xlsx

Iptopara.xlsx

testSeries1.xlsx

testseries2.xlsx

testseries3.xlsx

testsWithBond.xlsx

Model files:

test1.1GSResidual+C.gid

test1.1nointercCC.gid

test1.2GSResidual+C.gid

test1.3HnointercCC.gid

test1.4GSResidual+C.gid

test2.1GS.gid

test2.2GS.gid

test2.3GS.gid

test3.1GShalfInter.gid

test3.2GShalfInter.gid

test3.3GShalfInter.gid

test4.1HGS.gid

test4.2GS.gid

IPTO_a3dv1.gid

IPTO_b3dv5.gid

IPTO_c3NOSOFT.gid

APPENDIX A

Sliding stability analysis

A concrete dam is casted in sections. For stability analysis all of these sections must be evaluated, and all sections needs to be stable (NVE 2005). According to Johansson (2009) sliding can be described by two principally different types of sliding failure, Plane sliding and Wedge sliding. The mechanics are similar for both types, but the geometry of the wedge introduces 3D effects which makes this failure more difficult to assess analytically. In this section four methods for analyzing plane sliding stability are presented.

The sliding resistance method

In the sliding resistance method a friction coefficient μ is calculated by dividing the sum of horizontal forces on the sum of vertical forces. The calculated friction coefficient is compared to a limit value, an allowable friction coefficient μ_{all} , as shown in equation (3.1),

$$\mu = \frac{\sum H}{\sum V} \leq \mu_{all} \quad (A.1)$$

where μ is the friction coefficient, $\sum H$ the sum of horizontal forces, $\sum V$ the sum of vertical forces and μ_{all} is the allowed friction coefficient.

This method was widely used between the early 1900's and the 1930's (Johansson 2009), and is still used in Sweden today (Johansson 2012).

The shear friction method

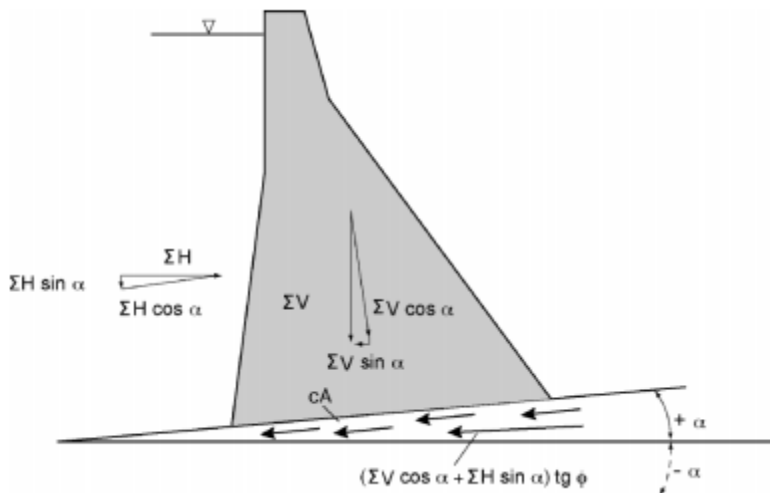
The shear friction method is the model used in the Norwegian guidelines today (NVE 2005). For a given sliding-plane, the principle for this method is to find a factor of safety (FS) by dividing the horizontal shear capacity, H_f , on the sum of horizontal forces, H , acting on the plane (Energi Norge 2012). The method can be described by the following equation:

$$FS = \frac{\sum H_f}{\sum H} \quad (A.2)$$

The shear capacity is calculated from the linear Mohr-Coulomb criterion, averaged over the area of the sliding-plane. For a horizontal sliding plane the method results in this equation for the factor of safety:

$$FS = \frac{c \cdot A + \sum V \cdot \tan \phi}{\sum H} \quad (\text{A.3})$$

Where FS is the factor of safety, c is the cohesive parameter of the sliding plane, A is the area of the sliding plane, ϕ is the friction angle, V and H is the vertical and horizontal forces respectively.



Sketch of the shear friction method for tilted sliding-plane (NVE 2005).

For a tilted sliding-plane with a tilt angle α , as shown in the figure equation (A.2) is rewritten, for derivation see Eltervaag (2012).

$$FS = \frac{\frac{c \cdot A}{\cos \alpha (1 - \tan \alpha \cdot \tan \phi)} + \sum V \cdot \tan(\alpha + \phi)}{\sum H} \quad (\text{A.4})$$

It should be noted that in this method only the *average* cohesion and tilt angle is taken into account.

The limit equilibrium method

The limit equilibrium method defines the factor of safety by dividing the tangential shear capacity, τ_f , on the acting *tangential* forces, τ , on the sliding plane (Energi Norge 2012). This is different from the shear resistance method, which refers to the horizontal forces acting on the sliding plane. The limit equilibrium method can be described using the following equation:

$$FS = \frac{\tau_f}{\tau} \quad (\text{A.5})$$

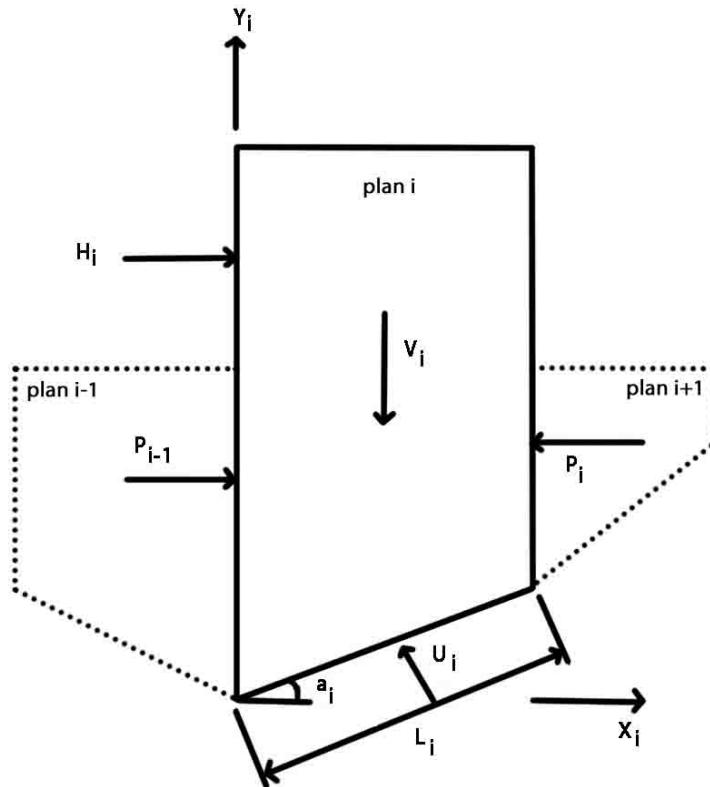
Nicholson (1983) described that this way of defining the factor of safety can be thought of as the degree of shear stress mobilized at the surface.

By applying the Mohr-Coulomb criteria to the limit equilibrium method the factor of safety can be derived from equilibrium into the following equation. For derivation see Eltervaag (2012).

$$FS = \frac{c \cdot A + \max |(\sum V \cdot \cos \alpha - \sum H \cdot \sin \alpha), 0| \cdot \tan \phi}{\text{abs} | \sum H \cdot \cos \alpha - \sum V \cdot \sin \alpha |} \quad (\text{A.6})$$

Where FS is the factor of safety, c is the cohesion of the sliding plane, A is the area of the sliding plane, ϕ is the friction angle of the plane, α is the tilting angle of the plane, V and H is the vertical and horizontal forces respectively. The maximum and absolute values are introduced to avoid negative factors of safety for negative vertical forces (upwards) or tangential forces (to the right in figure 3.1).

Nicholson (1983) also presented a method for assessing sliding on multiple sliding planes based on the limit equilibrium method. To apply this method the cross section is divided into n strips called wedges.



Principle sketch for the multiple sliding plane model (Stølen 2012).

It is then assumed that the factor of safety is equal for all the wedges, which implies that the structure is in equilibrium. This assumption gives n equations:

$$FS = FS_1 = FS_2 = \dots = FS_n \quad (\text{A.7})$$

The equilibrium also enables the establishment of equation for the resultants, P , acting on the wedges.

$$\sum_{i=1}^n (P_{i-1} - P_i) = 0 \quad (\text{A.8})$$

Instead of calculating each of these resultants, Nicholson (1983) presented an alternative iteration-based formulation, which gives the factor of safety for the whole system:

$$FS = \frac{\sum_{i=1}^n c_i \cdot A_i \cdot \cos \alpha_i + (V_i - U_i \cdot \cos \alpha_i) \cdot \tan \phi_i}{\sum_{i=1}^n (H_i - V_i \cdot \tan \alpha_i) n_{\alpha i}} \quad (\text{A.9})$$

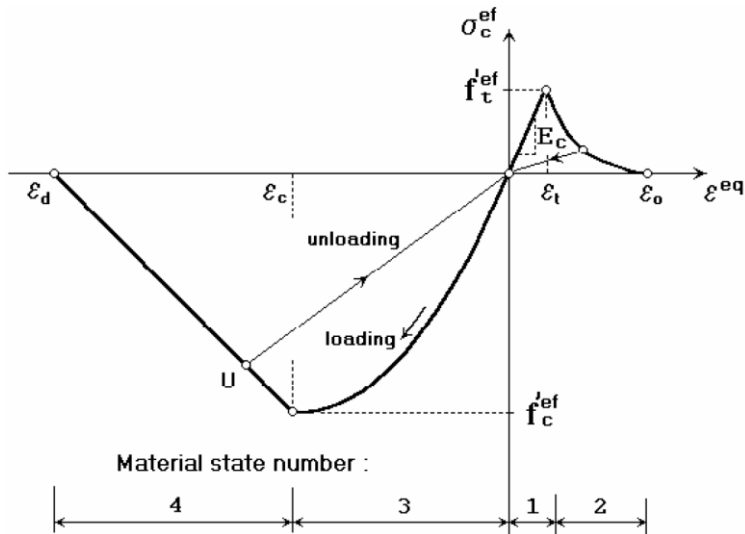
where $n_{\alpha i}$ is expressed as follows:

$$n_{\alpha i} = \frac{1 - \frac{\tan \phi_i \cdot \tan \alpha_i}{FS}}{1 + \tan^2 \alpha_i} \quad (\text{A.10})$$

APPENDIX B

Material models in Stølen's Master's Thesis

The materials was modeled using a fracture-plastic failure model (CC3DNonLinCementious2) developed by ATENA. The model contains sub-models for the concrete tensile and compressive behaviors and is illustrated in the figure below.



Stress-strain relationship for the concrete model. From Stølen (2012)

The reinforcement was modeled as separate bars with a bilinear stress-strain relationship. It was chose not to include models for bond between the concrete and the rebars, but instead use conservative values for the yielding limit of the reinforcement steel.

The rock material is modeled using the Drucker-Prager criterion, which Stølen (2012) expresses on the form

$$f(I_1, \sqrt{J_2}) = \sqrt{J_2} - \alpha I_1 - k = 0 \quad (B.1)$$

Where I_1 and J_2 are the first and second deviatoric invariants of the stress-tensor, and α and k are constants related to the cohesive and frictional parameters in the Mohr-Coulomb criterion.

In the tables below the material parameters used by Stølen is listed.

Material parameters from Stølen (2012)

Material parameter	Concrete	Rock	reinforcement
Young's Modulus [GPa]	32	30	-
Poisson number	0.2	0.2	-
Density [kN/m ³]	23	27	-
Compressive strength [MPa]	30	50	-
Tensile strength [MPa]	2	10	-
Yield strength [MPa]	-	-	170
Strain at tensile failure	-	-	0.025

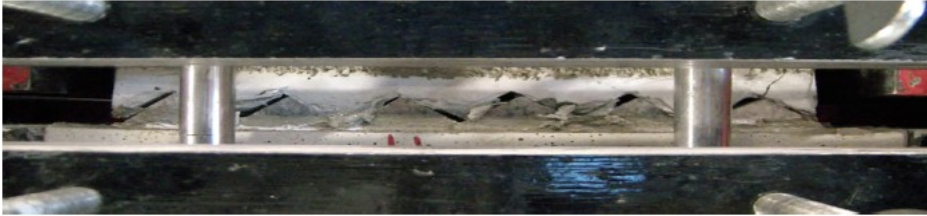
Material parameters for interface elements. From Stølen (2012)

Material parameters for the interface material	
ϕ^8 [°]	38
Cohesion [MPa]	Varying
K_{nn} [MN/m ³]	1.5×10^7
K_{nn}^{\min} [MN/m ³]	6.25×10^6
K_{tt} [MN/m ³]	15×10^3
K_{tt}^{\min} [MN/m ³]	6.25×10^3

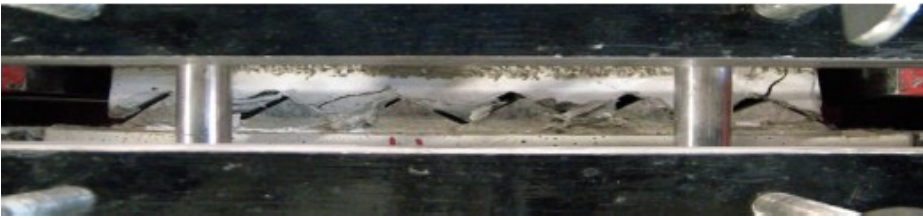
⁸ This is the basic friction angle, which in this Thesis is denoted ϕ_b . For convenience the symbol used by Stølen is kept in this table.

APPENDIX C

Pictures of the direct shear tests conducted by Simen Liahagen at LTU in 2012



Test 1.1 at maximum capacity after approximately 4mm displacement



Test 1.1 after approximately 5mm displacement



Test 1.1 after maximum displacement. Approximately 15mm



Test 1.2 at maximum capacity after approximately 3mm displacement



Test 1.2 after approximately 5mm displacement



Test 1.2 after maximum displacement. Approximately 15mm



Test 1.3H at max capacity.



Test 1.3H after maximum displacement. Approximately 15mm



Test 1.4 at maximum capacity after approximately 1.4mm of displacement



Test 1.4 after approximately 5mm displacement



Test 1.4 after maximum displacement. Approximately 26mm



Test 2.1 at maximum capacity after approximately 6.4mm of displacement



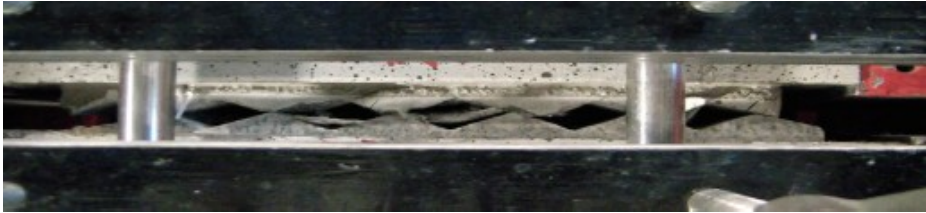
Test 2.1 after approximately 15mm displacement



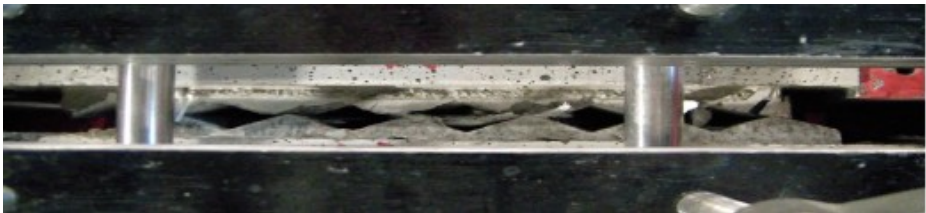
Test 2.1 after maximum displacement. Approximately 25mm



Test 2.2 at maximum capacity after approximately 2.9mm of displacement



Test 2.2 after approximately 15mm displacement



Test 2.2 after maximum displacement. Approximately 22mm



Test 2.3 at maximum capacity after approximately 2.3mm of displacement



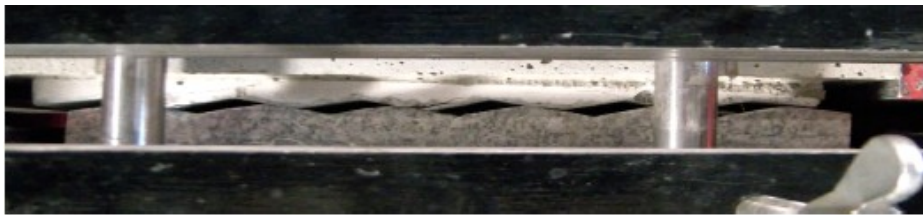
Test 2.3 after approximately 5mm displacement



Test 2.3 after approximately 15mm displacement



Test 2.3 after maximum displacement. Approximately 20mm



Test 3.1 at maximum capacity after approximately 9.8mm of displacement



Test 3.1 after maximum displacement. Approximately 33mm



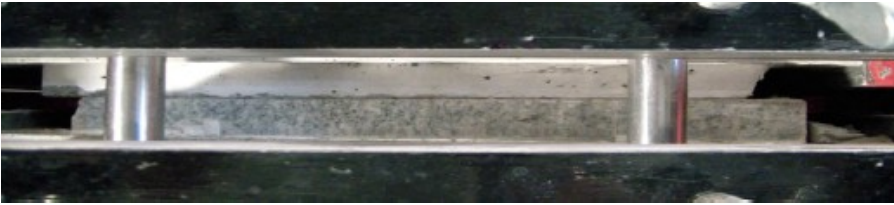
Test 3.3 at maximum capacity after approximately 2.8mm of displacement



Test 3.3 after maximum displacement. Approximately 33mm



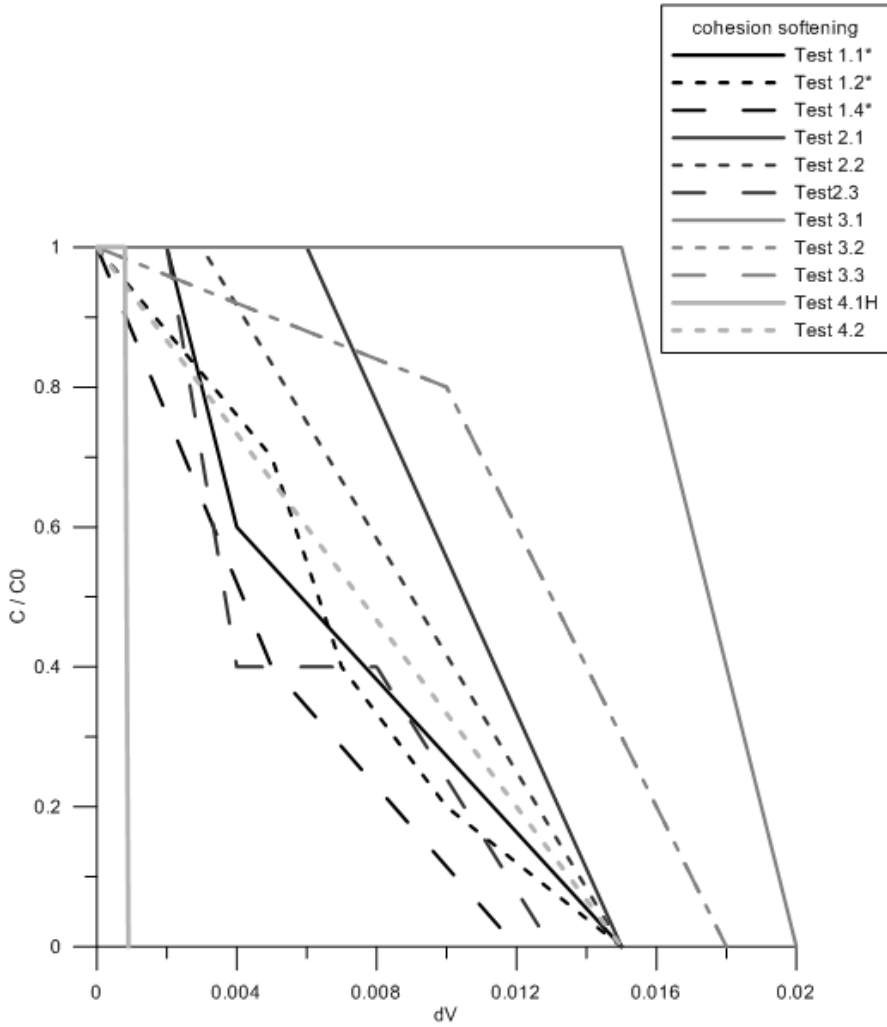
Test 4.1H after approximately 15mm of deformation



Test 4.2 after approximately 33mm of deformation

APPENDIX D

Softening functions from the numerical analyses.



APPENDIX E

Description of the CCxDNonLinCementitious material model.

The descriptions in this section have been found in the ATENA Theory manual and are somewhat compacted. Thus, for further details consult the Theory manual (Cervenka et. Al 2012).

The material model formulation is based on decomposing the strain into elastic, ε^e , plastic, ε^p , and fracturing, ε^f , parts.

$$\varepsilon_{ij} = \varepsilon_{ij}^e + \varepsilon_{ij}^p + \varepsilon_{ij}^f \quad (\text{E.1})$$

The stress state is updated according to:

$$\sigma_{ij}^n = \sigma_{ij}^{n-1} + E_{ijk} (\Delta \varepsilon_{kl} - \Delta \varepsilon_{kl}^p - \Delta \varepsilon_{kl}^f) \quad (\text{E.2})$$

Constitutive model for tensile behavior

The model uses the Rankine-fracturing model for concrete cracking to describe the tensile behavior of concrete. It is assumed that strains and stresses are converted into material direction, i , such that the failure criterion⁹ can be given in the following form.

$$F_i^f = \sigma_{ii}' - f_{ii}' \leq 0 \quad (\text{E.3})$$

Where σ_{ii}' is the trail stress, and f_{ii}' is the tensile strength. $F = 0$ indicates cracking. The trail stress is computed by an elastic predictor:

$$\sigma_{ij}' = \sigma_{ij}^{n-1} + E_{ijkl} \Delta \varepsilon_{kl}' \quad (\text{E.4})$$

If the calculated trail stress does not satisfy equation 5.1 the increment of fracture strain in direction i can be computed by assuming that the final stress must satisfy:

$$F_i^f = \sigma_{ii}' - f_{ii}' = \sigma_{ii}' - E_{ijkl} \Delta \varepsilon_{kl}' - f_{ii}' = 0 \quad (\text{E.5})$$

⁹ Failure occurs as the value of F equals zero. This can be illustrated graphically as a three dimensional object. Either you are inside the object (no failure) or you are on the surface (failure). A positive value of F (outside the object) is unphysical.

This equation may be simplified by utilizing the assumption that the increment of fracture strain is orthogonal to the failure surface being checked. For failure surface k , the incremental fracture strain has the following form.

$$\Delta \varepsilon_{ij}^f = \Delta \lambda \frac{\partial F_k^f}{\partial \sigma_{ij}} = \Delta \lambda \delta_{ik} \quad (\text{E.6})$$

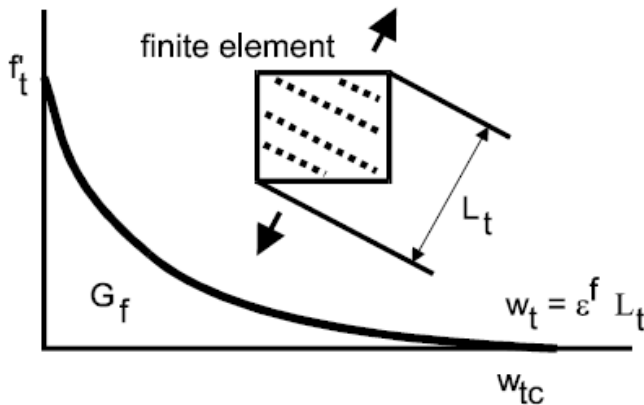
Incremental fracturing multiplier, λ , is obtained by substituting equation E.6 into equation 5.5.

$$\Delta \lambda = \frac{\sigma_{kk}^t - f_{tk}^t}{E_{kkkk}} = \frac{\sigma_{kk}^t - f_t^t(w_k^{\max})}{E_{kkkk}} \quad (\text{E.7})$$

This equation must be solved by iteration, since for softening materials the current tensile strength $f_t^t(w_k^{\max})$ is dependent on the crack opening, w . The crack opening is computed from the sum of total fracturing strain $\hat{\varepsilon}_{kk}^f$ in direction k plus the current fracture strain increment, $\Delta \lambda$, multiplied with the characteristic length L_t .

$$w_k^{\max} = L_t (\hat{\varepsilon}_{kk}^f + \Delta \lambda) \quad (\text{E.8})$$

The characteristic length can be seen as the size of the element projected into the crack direction.



Sketch of characteristic length. (Cervenka et. Al 2012)

Shear strength of cracked concrete is found using a modified Compression Field Theory

$$\sigma_{ij} \leq \frac{0.18\sqrt{f'_c}}{0.31 + \frac{24w}{a_g + 16}}, \quad i \neq j \quad (\text{E.9})$$

Where f'_c is the compressive strength in MPa, a_g is the maximum aggregate size and w is the maximum crack width in mm at the given location. By applying the maximum aggregate size the user allows the shear stress at the cracks to exceed the tensile strength. If the aggregate size is not specified, the tensile strength is the default value for maximal shear stress.

Constitutive model for compressive behavior

To model the compressive behavior of concrete the model uses a plasticity model for concrete crushing. This model computes the new stress state by a predictor-corrector formulation.

$${}^{(n)}\sigma_{ij} = {}^{(n-1)}\sigma_{ij} + E_{ijkl}(\Delta\varepsilon_{kl} - \Delta\varepsilon_{kl}^p) = \sigma_{ij}^t - E_{ijkl}\Delta\varepsilon_{kl}^p = \sigma_{ij}^t - \sigma_{ij}^p \quad (\text{E.10})$$

The plastic corrector σ_{ij}^p is computed directly from the yield function by a return mapping algorithm

$$F^p(\sigma_{ij}^t - \sigma_{ij}^p) = F^p(\sigma_{ij}^t - \Delta\lambda l_{ij}) = 0 \quad (\text{E.11})$$

Where l_{ij} is the return direction, defined as:

$$l_{ij} = E_{ijkl} \frac{\partial G^p(\sigma_{kl}^t)}{\partial \sigma_{kl}} \quad (\text{E.12})$$

Where $G(\sigma_{ij})$ is the plastic potential function. The derivative of this is evaluated at the predictor stress, σ_{ij}^t , to determine the return direction. Finally the following failure surface, first described by Men eterey and William (Cervenka et. Al 2012), is applied.

$$F_{3P}^p = \left[\sqrt{1.5} \frac{\rho}{f'_c} \right]^2 + m \left[\frac{\rho}{\sqrt{6}f'_c} r(\theta, e) + \frac{\xi}{\sqrt{3}f'_c} \right] - c = 0 \quad (\text{E.13})$$

Where

$$m = 3 \frac{f_c'^2 - f_t'^2}{f_c' f_t'} \frac{e}{e+1} \quad \text{and} \quad r(\theta, e) = \frac{4(1-e^2)\cos^2\theta + (2e-1)^2}{2(1-e^2)\cos\theta + (2e-1) \left[4(1-e^2)\cos^2\theta + 5e^2 - 4 \right]^{\frac{1}{2}}}$$

In the above equations (ζ, ρ, θ) are cylindrical coordinates (also referred to as Haigh-Westergaards coordinates), f_c' and f_t' is the compressive and tensile strength respectively. The parameter $e \in \langle 0.5, 1.0 \rangle$ describes the roundness of the failure surface, for $e=0.5$ the corners are sharp, and for $e= 1.0$ the failure surface is completely circular.

The position of the failure surface depends on the value of strain hardening/softening, which is based on the equivalent plastic strain, ε_{eq}^p . The change in equivalent plastic strain, $\Delta \varepsilon_{eq}^p$, is calculated as follows.

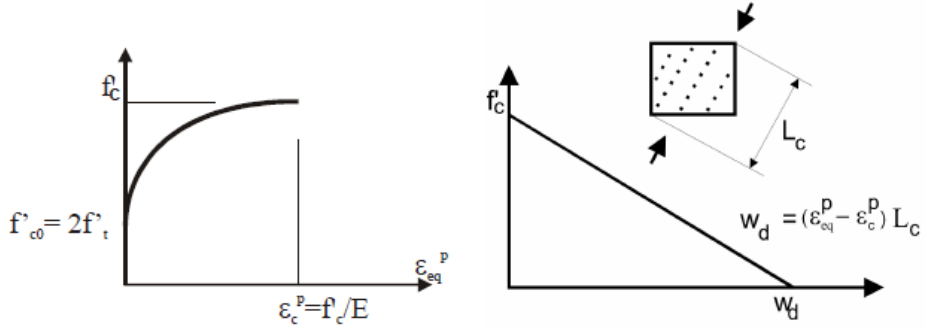
$$\Delta \varepsilon_{eq}^p = \min(\Delta \varepsilon_{ij}^p) \quad (\text{E.14})$$

For the Menéterey-Williams failure surface the hardening/softening is described by the $c \in \langle 0, 1 \rangle$, which can be expressed by the following relation

$$c = \left(\frac{f_c'(\varepsilon_{eq}^p)}{f_c'} \right)^2 \quad (\text{E.15})$$

Above the hardening/softening law is expressed by f_c' which is based on uniaxial compressive tests. This law is illustrated in the figure **Error! eference source not found.** below with a linear softening curve and an elliptical ascending part described by.

$$\sigma = f_{co} + (f_c - f_{co}) \sqrt{1 - \left(\frac{\varepsilon_c - \varepsilon_{eq}^p}{\varepsilon_c} \right)^2} \quad (E.16)$$



Compressive hardening/softening (Cervenka 2012)

This hardening/softening law is based on the work of Van Mier (Cervenka 2012).

Combining the two models

As mentioned in the intro, the material model combines both of the described methods to model concrete. Generally this is done by solving the two following inequalities simultaneously

$$F^p \left({}^{(n-1)}\sigma_{ij} + E_{ijkl} (\Delta\varepsilon_{kl} - \Delta\varepsilon_{kl}^f - \Delta\varepsilon_{kl}^p) \right) \leq 0 \text{ solve for } \Delta\varepsilon_{kl}^p \quad (E.17)$$

$$F^f \left({}^{(n-1)}\sigma_{ij} + E_{ijkl} (\Delta\varepsilon_{kl} - \Delta\varepsilon_{kl}^p - \Delta\varepsilon_{kl}^f) \right) \leq 0 \text{ solve for } \Delta\varepsilon_{kl}^f \quad (E.19)$$

These inequalities are interdependent, and therefore results are obtained through iteration. For iteration schemes and iteration convergence criteria see the Theory manual (Cervenka 2012).

APPENDIX F

The interface stiffness used in the parametric study was calculated as follows.

$$K_{mn} = \frac{E_{rock}}{t_{element}} \cdot M \quad (F.1)$$

$$K_{tt} = \frac{G_{rock}}{t_{element}} \cdot M \quad (F.2)$$

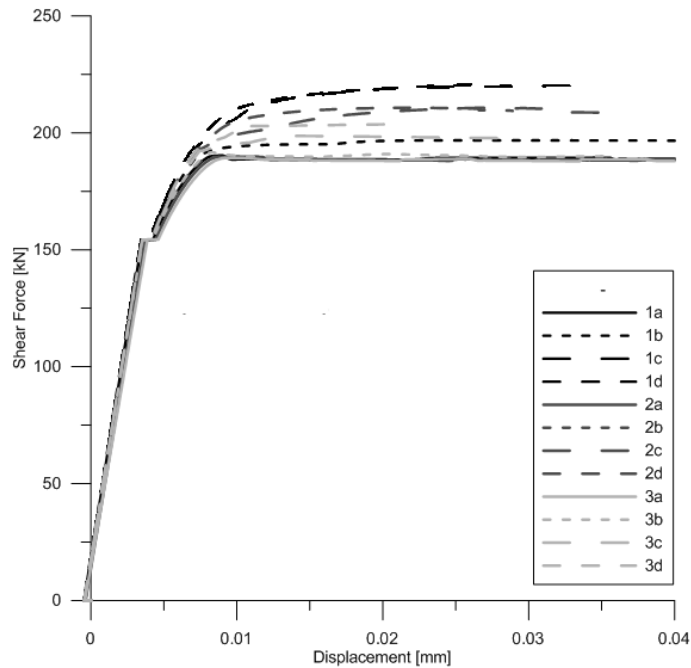
Where $t_{element}$ is the size of the interface elements, and M is a multiplier varying from 1 to 100. The G-modulus can be found as

$$G = \frac{E}{2 \cdot (1 + \mu)} \quad (F.3)$$

In order to present the results from this study in a convenient way, the analyses were given numbers. These numbers were given according to the combination of element size and multiplier, and the relation is shown in the table below

Element size [m]	M=1	M=10	M=50	M=100
0.1	1a	1b	1c	1d
0.2	2a	2b	2c	2d
0.4	3a	3b	3c	3d

The result of this parametric study is shown in the figure below.



Load displacement diagram of the parametric study

From this parametric study it is seen that the element stiffness is affecting the shear capacity. Since no tests of the exact shear capacity for a horizontal sliding plane exist, the lowest value of K_{nn} and K_{tt} are chosen. The lowest shear capacity is found from analysis 3a, thus this mesh size and element stiffness is used for the further analyses.

APPENDIX G

Conditional break criteria can be set to stop the computation if an error exceeds the prescribed tolerance multiplied by the prescribed factor during the iterations or at the end of an analysis step (Cervenka et. Al 2013).

For the analyses run in this Thesis the multiplier is set to 20, and default values for the error tolerances in the convergence criteria are kept.

The multiplier 20 means that the analysis stops if the error exceeds the tolerance 20 times. Below is an example with 1% tolerance (default), 20 multiplier, max 60 iterations:

error < 0.01 in 60 or less iterations - no exclamation mark, analysis continues with the next step

0.01 < error < 0.20 in iteration 60 - exclamation mark, analysis continues with the next step

0.20 < error in iteration 60 - exclamation mark, analysis stops